

# Analysis of the seasonal velocity difference of the Greenland Russell glacier using multi-sensor data

Ya-Lun S. Tsai<sup>1</sup>, Shih-Yuan Lin<sup>1</sup>, Jung-Rack Kim<sup>2,\*</sup>, and YunSoo Choi<sup>2</sup>

<sup>1</sup>Department of Land Economics, National Chengchi University, Taipei City, Taiwan

<sup>2</sup>Department of Geoinformatics, University of Seoul, Seoul, Korea

## Article history:

Received 24 December 2017

Revised 28 April 2019

Accepted 3 June 2019

## Keywords:

Greenland ice sheet, Glacier, InSAR, Offset tracking, Numerical ice sheet model, Subglacial features

## Citation:

Tsai, Y.-L. S., S.-Y. Lin, J.-R. Kim, and Y. Choi, 2019: Analysis of the seasonal velocity difference of the Greenland Russell glacier using multi-sensor data. *Terr. Atmos. Ocean. Sci.*, 30, 541-562, doi: 10.3319/TAO.2019.06.03.01

## ABSTRACT

To fulfil the strong need for monitoring seasonal difference of velocity over the Greenland ice sheet (GrIS), we developed an approach based on the fusion of multiple temporal and multi sensor remote sensing observations. We used spaceborne synthetic aperture radar (SAR) and optical data over the Russell glacier in southwestern Greenland. Firstly, offset tracking and InSAR time series analyses were employed for deriving the glacier's velocity in planimetric and line of sight (LOS) directions. Next, a three-dimensional (3D) decomposition was applied for estimating the 3D velocity vectors of the glacier. Once the reliability of the results was validated, a numerical ice sheet model (ISM) was further applied to derive the modelled basal friction in different seasons. We concluded that the overall data integration using multiple open-accessed satellite image employed in this study demonstrated a decent method to analyze seasonal velocity difference of the Russell glacier. Based on the proposed monitoring strategy, it is of great potential to further investigate other polar and inland glaciers with various remote sensed data.

## 1. INTRODUCTION

Global warming is a worldwide phenomenon that significantly increases the melting rate of the icecaps in the polar regions, which elevates the sea level, thus posing a fundamental threat (Jevrejeva et al. 2014; Nicholls et al. 2014). Because the Greenland ice sheet (GrIS), as the second largest ice sheet in the world, contains more than 2.85 million cubic kilometers of ice (Weidick 1995), it is estimated to be the critical contributor to the rising sea level, potentially contributing around 7.4 m to the sea level if totally melted into water (Bamber et al. 2013; Hanna et al. 2013). Owing to the global warming, the rapid melting rate and a significant loss of mass of the GrIS have been observed (Shepherd et al. 2012; Khan et al. 2014). To track the melting dynamics, continuous monitoring of GrIS is critical and such monitoring has been conducted globally and locally by various international science missions. For instance, the Greenland Ice Sheet Climate Change Initiative

(CCI) project, conducted by the European Space Agency (ESA), employed multiple sensors to monitor the calving front location, the ice velocity, changes in the surface elevation, and grounding line location; this monitoring started in 1991 and is ongoing.

Based on the experiments conducted in Greenland, it was found that the mass loss of the GrIS is highly correlated with the glacier velocity. Therefore, monitoring the velocity of the glacier terminus is an effective way to estimate the mass loss and to further understand the impact of the climate change (Mattar et al. 1998; Strozzi et al. 2008; Khan et al. 2014). To achieve quantitative monitoring of the glacier terminus, various geomatics techniques, specializing in observations of ground surface changes, have been suggested. However, there are challenging environment conditions such as remarkably homogeneous landscape, relatively fast glacier velocity, unstable surface ice, and snow meltdown and accumulation conditions (Strozzi et al. 1999, 2002). Consequently, observations through GNSS surveying (Barrand et al. 2009; Karpilo 2009; Ke et al. 2013) or

\* Corresponding author  
E-mail: kjrr001@gmail.com

photogrammetry (Baltsavias et al. 2001; Käab et al. 2002; Quincey et al. 2005) have been constrained.

Considering the aforementioned limitations, remote sensing using multiple spaceborne images remains the most advantageous method for extraction of information on glacial dynamics (Huang and Li 2011; Rignot and Mouginot 2012; Robson et al. 2015; Joughin et al. 2016). Since the launch of the Landsat series satellite in the 1970s, countries and institutes all over the world have contributed to various satellite missions. Together with the development, the optical and synthetic aperture radar (SAR) spaceborne images with better spatial and temporal resolution accessible from public domain has been significantly increasing in recent years. For example, the latest Landsat-8 satellite launched on February 2013 has 12-bit radiometric quantization with 16-day repeat cycle, which uses an operational land imager (OLI) sensor instead of an enhanced thematic mapper plus (ETM+) sensor that was used in earlier instruments, ensuring that ground details can be recorded up to 15 m spatial resolution. For the purpose of glacier velocity tracking, due to the rectification and orbital accuracy, Landsat-8 also demonstrated advanced accuracy comparing to other accessible optical sensors such as Advanced Spaceborne Thermal Emission and Reflection Radiometer (ASTER) and Sentinel-2 (Tsai et al. 2018). Meanwhile, regarding the accessible SAR imagery, the C-band Sentinel-1 twin satellites launched by ESA on April 2014 and 2016 have a ground resolved distance (GRD) of about 5 m × 20 m, with a revisit period of 12 days, which is also publicly available in near real-time. The potential of using Sentinel-1 for cryosphere monitoring has been thoroughly discussed in Sentinels for Science (SEN4SCI) scientific workshop (Malenovsky et al. 2012) and has been employed frequently in recent studies (Nagler et al. 2016; Tsai et al. 2019).

Although such high quality spaceborne imaging assets enable the continuous monitoring of specific glacier areas with improved spatial and temporal resolutions, it should be noted that imaging characteristics of spaceborne assets have to be compensated by multi-sensor data integration. For instance, poor visibility in cloud as well as temporal and spatial baseline issues limit the potential of in-time observations of fast moving glacier based on optical and SAR sensor, respectively. Thus multiple optical and SAR images should be employed simultaneously. Furthermore, an extraction of three-dimensional glacier velocity for investigating comprehensive glacial dynamics was another reason that fusion of glacier velocity of different directions sensed by SAR and optical sensors was critical. Based on the derived velocity, a precise quantitative modelling of the glacier terminus could then be achieved. In this study, we therefore proposed to integrate Landsat-8 optical and Sentinel-1 SAR image data to monitor one of the most well-known land-terminating glaciers in Greenland, the Russell glacier. We mainly focused on proposing a feasible method

to extract the glacier terminus seasonal three-dimensional velocity. Furthermore, in order to demonstrate the potential of the derived remote sensing observation, a numerical ice sheet model representing the dynamics of the target glacier was established. The remote sensing processing techniques applied, the assessment and the results were following introduced. A preliminary interpretation of the friction condition of ice/bedrock interface derived from mathematical modelling compared to remote sensing observations was also discussed hereafter.

## 2. TARGET AREA AND DATA SETS

### 2.1 Target Area

The proposed monitoring strategy was applied for observations of the area in the southwestern ablation zone of the GrIS, mainly covering the Isunnguata Sermia, Russell, Leverett, Ørkendalen, and Isorlersuup glaciers (Fig. 1), which is one of the most scientifically interesting areas over the entire GrIS (Zwally et al. 2002; Joughin et al. 2008; Van de Wal et al. 2008; Bartholomew et al. 2010). Addition to the scientific value of this area, since all of these glaciers are land-terminating glaciers which are independent from the tidal and calving effect, and are being at the edge of the GrIS, where the most significant indicators of changes in the GrIS are located. Hence, the relatively simple glacier dynamics ensures the application and validation of our monitoring approach. Observations such as surface mass balance, changes in supraglacial lakes and ice sheet dynamics, have been conducted by previous studies (Van de Wal et al. 2008; Bartholomew et al. 2011; Palmer et al. 2011; Sole et al. 2013). Previous studies have been conducted to measure the velocity of ice over entire Greenland, including the Russell glacier area (Joughin et al. 2010; Moon et al. 2012; Rignot and Mouginot 2012; Tedstone et al. 2014). However, after 2013 no studies have reported observations of 3D glacial velocity in different seasons of the target area with fine (< 1 km) spatial resolution, in spite of the importance of this area in the studies of glacial velocity.

### 2.2 Data Sets

The strategy proposed in this study amounts to using the latest optical and SAR images with offset tracking and InSAR time-series algorithms. The study bears the promise to fill the temporal gap and enable continuous monitoring of the ice velocity and dynamics in the target area.

#### 2.2.1 Sentinel-1 and Landsat-8

For SAR images, the latest ESA C-band Sentinel-1 images were used in this study. We selected images in the interferometric wide swath (IW) mode, which corresponds to the terrain observation with progressive scans in azimuth

(TOPS). This image acquisition mode is able to achieve wide image coverage as ScanSAR mode does, but also can reduce the scalloping effect and to maintain a high-quality signal-to-noise (SNR) ratio along the flight direction as a full azimuth antenna is used (De Zan and Guarneri 2006; Meta et al. 2010; Geudtner and Torres 2012; Torres et al. 2012). This setting ensures the along-track and cross-track uncertainties are within 50 m and 10 m at the  $1\sigma$  level. Its high spatial resolution (4 m  $\times$  14 m) guarantees that the glacier surface can be detected in detail. The intensity information stored in the level 1 single look complex (SLC) product was selected, and the HH polarization was chosen for its high SNR and better quality of ground features (Nagler et al. 2015).

The band 8 (panchromatic) channel with the resolution of 15 m in Landsat-8 data was chosen for offset tracking processing. To acquire ortho-rectified images, the L1T (precision ortho-corrected product with GCPs and DEMs) product was used, which ensures that the uncertainty of geodetic pixels is under 12 m and the band-to-band co-registration is under 4.5 m, at the 90% level of confidence (Storey et al. 2014).

The SAR Sentinel-1 and optical Landsat-8 images covering summertime and wintertime of 2016 were proposed to be used to estimate the displacement over the Russell glacier in different seasons. Unfortunately, as the cloud coverage of Russell glacier dominated most of the images in 2016, there was no proper Landsat-8 image could be used in wintertime while only one pair was available in summertime. Consequently, time-series Sentinel-1 images were employed for wintertime and one pair of Sentinel-1 images was selected for summertime accordingly. The specifications of summertime and wintertime satellite images used in this study are summarized in Tables 1 and 2, respectively.

### 2.2.2 Complementary Data

To compare with the resultant surface glacier velocity, due to the difficulty of finding suitable ground truth covering the same temporal and spatial scale of remote sensing-based product, we used the ice velocity data provided by ESA's Greenland Ice Sheet CCI project (<http://products.esa-icesheets-cci.org/products/downloadlist/IV>) instead. It provides 500-m-resolution gridded velocity and a 1-year static average computed from October of 2015 to October of 2016. Although it did not exactly match our studying period and was with coarse resolution compared with our results, the overall spatial pattern and magnitude of glacier velocity was clear and comparable in this study.

Furthermore, because subglacial topography is regarded as an indispensable factor of glacier dynamics and melt-water storage (Rennermalm et al. 2013; Smith et al. 2015) as well as thermal transfer and lubrication of ice sheet which affect the glacier velocity (Hanna et al. 2008; Cuffey and Paterson 2010), the bedrock topography and the ice thick-

ness data derived from NASA's Operation IceBridge (OIB) mission (Morlighem et al. 2014, 2015) as well as the surface temperature provided by Ettema et al. (2009) which included in the Sea-level Response to Ice Sheet Evolution (SeaRISE) project (Bindshadler et al. 2013) were used in parallel with our results for further analysis. The OIB ice thickness was extracted using a radar sounding technique, and bedrock topography was obtained by subtracting the ice thickness from the surface DEM further deduced. The spatial resolution is 150 m, which is quite similar to that of our study, so a comparison can be performed.

### 3. PROCESSING METHOD

Given the availability of high-quality spaceborne images, in this study we investigated the feasibility of tracking the dynamic behavior of local terminus using multiple high-resolution datasets. Basically, we used two remote sensing methods to detect the velocity of the glacier surface: the offset tracking [pixel offset (PO)] method, and the InSAR time series analysis method.

Firstly, the PO technique was based on the normalized cross-correlation (NCC) algorithm for tracking the distance between glacial features across different images. Owing to the image normalization, differently illuminated images can be compared (Heid and Käab 2012). After processing, the line-of-sight (LOS) and azimuth direction displacements were estimated for a pair of SAR images, while displacements in the Easting and Northing directions were derived using the ortho-rectified pair of optical images. In this study, the SAR images were processed using offset tracking but not using the conventional D-InSAR technique. This was inferred from the monitoring tasks conducted in previous studies (Massonnet and Feigl 1998; Baran et al. 2005; Zhou et al. 2011). Owing to the rapid deformation of the glacier, especially in summer time and quick changes in the meteorological and glacier flow conditions, the coherence of the SAR image pairs reduced significantly, making conventional D-InSAR processing non-applicable. Instead, offset tracking is a relatively feasible method and has been widely applied for monitoring of glacier displacement (Gray et al. 1998, 2001; Michel and Rignot 1999; Pattyn 1999). Especially the snow free glacial texture in summer time provided ideal condition for the application of NCC-based PO. Thus, this method was used in the present study to trace summer time glacial migration.

In addition to the offset tracking, to overcome the conventional incoherence-caused error occurred in D-InSAR, we employed the time series InSAR technique. It can not only extract partially coherent pixels from the interferogram stack but also correct both atmospheric and orbital error fringes. It should be noted that relative slow winter time glacial migration gives better phase coherence formation than summer time cases do. On the contrary, PO is not applicable

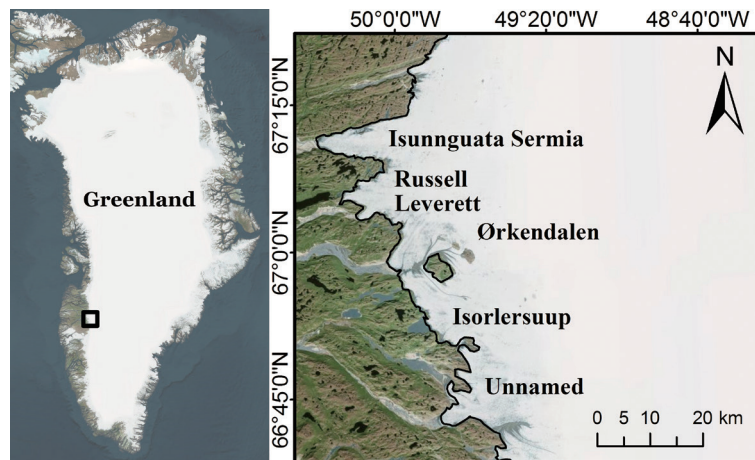


Fig. 1. The location of the test site, Russell glacier area, is outlined by the black box in the south-western ablation zone of Greenland. The positions of the five monitored glaciers are shown in the zoomed-in window with black outlines, which are digitized based on the boundary shown in the summertime optical image.

Table 1. Specifications of Landsat-8 and Sentinel-1A images acquired in summertime.

Sensor	Acquisition Date	Path	Row	Pass
Landsat-8	10 July 2016	7	13	Descending
Landsat-8	26 July 2016	7	13	Descending
Sensor	Acquisition Date	Cycle number	Orbit number	Pass
Sentinel-1A	16 July 2016	84	77301	Descending
Sentinel-1A	28 July 2016	85	12347	Descending

Table 2. Specifications of Sentinel-1A and Sentinel-1B images acquired in wintertime.

Sensor	Acquisition Date	Cycle number	Orbit number	Perpendicular baseline (m)	Pass
Sentinel-1A	30 September 2016	90	13287	72.57	Ascending
Sentinel-1B	06 October 2016	20	2391	-22.63	Ascending
Sentinel-1A	12 October 2016	91	13462	16.21	Ascending
Sentinel-1B	18 October 2016	21	2566	42.62	Ascending
Sentinel-1A	24 October 2016	92	13637	-70.36	Ascending
Sentinel-1B	30 October 2016	22	2741	77.54	Ascending
Sentinel-1A	05 November 2016	93	13812	-41.05	Ascending
Sentinel-1B	11 November 2016	23	2916	0	Ascending
Sentinel-1A	17 November 2016	94	13987	-6.36	Ascending
Sentinel-1B	23 November 2016	24	3091	-15.51	Ascending
Sentinel-1A	29 November 2016	95	14162	97.83	Ascending
Sentinel-1B	05 December 2016	25	3266	-46.59	Ascending
Sentinel-1A	11 December 2016	96	14337	69.47	Ascending
Sentinel-1B	17 December 2016	26	3441	-7.19	Ascending
Sentinel-1A	23 December 2016	97	14512	-5.40	Ascending
Sentinel-1B	29 December 2016	27	3616	92.69	Ascending

for the texture less snow covered surface in winter season. Moreover, the C-band Sentinel-1 SAR was found to be capable to penetrate dry snow cover (which usually exists in wintertime) around 20 m till surface of glacier (Mätzler 1987). However, when snow becomes wet in summertime, due to melting, the penetration depth significantly shrinks to 3 cm (Ulaby et al. 1986; Shi and Dozier 1995) caused by dielectric constant changing (Arslan et al. 2001). Hence, accurate long-term glacial surface LOS velocity measurements can be performed for measuring winter time glacial migration.

Furthermore, based on displacement in different directions calculated using various techniques, we performed a 3D decomposition to derive the local Cartesian displacement (ENU) (Hanssen 2001). Using the ENU vectors, the glacier displacement in the vertical direction can be inverted for further investigation. We therefore propose to apply the offset tracking and 3D decomposition methods for monitoring the displacement and 3D dynamics of local terminus. The overall data processing flow was given in Fig. 2.

### 3.1 InSAR Time Series Analysis

For long-term monitoring of glacial surface displacement, we processed a stack of SAR images using the optimal strategy, as shown in Fig. 2. First, we focused the images using the ESA sentinel application platform (SNAP) to obtain single-look-complex (SLC) images. Next, the conventional D-InSAR pairs were built in a continuous and chronological order to maintain the shortest temporal baseline for reliable coherence. Consequently, there was no redundancy in the pairs of images. To obtain a geocoded unwrapped interferogram and coherence map for each pair, the SNAP (Chen 2001) algorithm was used.

As conventional D-InSAR would largely limited by

the quick glacier motion and landscape changing, for time-series analysis we used the generic InSAR analysis toolbox (GIANt) software instead, which is capable of handling various D-InSAR outcomes and extracting partial coherent pixel to estimate final velocity. Additionally, it also provides the atmospheric and orbital correction module to ensure the reliability of result velocity outcome (Agram et al. 2013). The maps were first stacked in the GIANt in the netcdf format in order, and processed using the PyAPS (Jolivet et al. 2011) module for the atmospheric correction. The module automatically downloaded the ERA-Interim data from the European Center for Medium-Range Weather Forecast (ECMWF) (Dee et al. 2011) that were closest to the date of each scene, and used temperature and relative humidity at each height layer to estimate and remove atmospheric delays; this was applied to each D-InSAR pair. The topographic error was eliminated using the Greenland Mapping Project (GIMP) Digital Elevation Model (Korona et al. 2009), and the orbital error was mitigated using the GIANt de-ramp module, which used least squares to estimate an orbital fringe for each pair and linearly resolved the errors in the entire stack (Biggs et al. 2007; Cavalié et al. 2008). The InSAR time series algorithm was used owing to its capability to interpolate time series pixel displacement in the interferogram stack (López-Quiroz et al. 2009). Based on the resultant points, the average velocity and displacement trends for the period of study could be extracted.

### 3.2 Offset Tracking

To extract two-dimensional surface displacements, the offset tracking technique was also used on both SAR and optical images. For SAR images, because the SLC mode images look elongated for different resolutions in the azimuth/

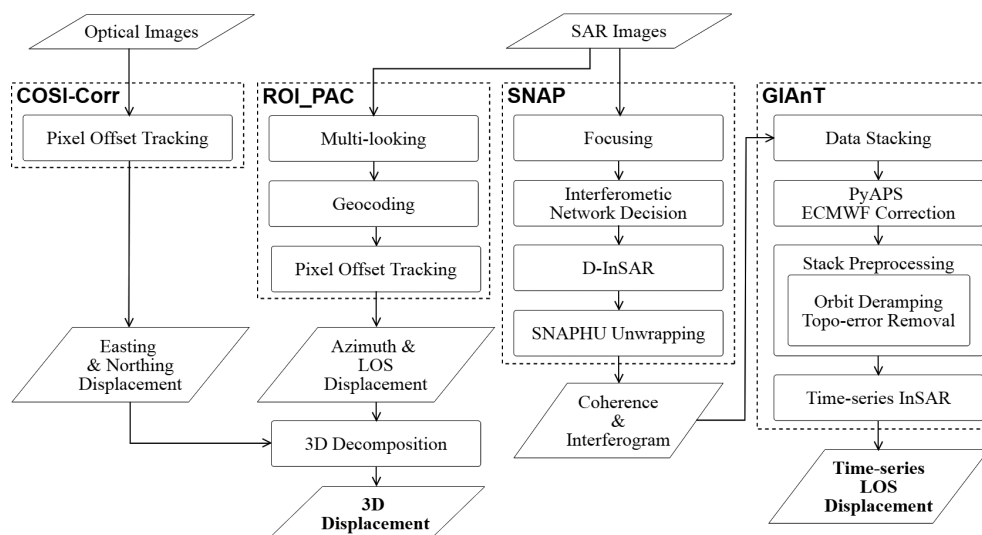


Fig. 2. The overall workflow and the output products from PO and InSAR time-series analysis.

range direction, and also suffer from the speckle effect, the multi-looking step was firstly applied to obtain an averaged spatial resolution and to reduce speckles (Henderson and Lewis 1998). Rather than amplitude images, the backscattering coefficient is optimal for precise measurements, because it significantly reduces the range of reflectance for all pixels, eliminating the possibility of wrong co-registration (Chan and Peng 2003). In addition, we found that co-polarized processing yields a better supraglacial feature delineating ability and a higher SNR, consistent with theoretical calculations (Nagler et al. 2015). After pre-processing that included multi-looking as well as geocoding, offset tracking was conducted using the “ampcor” approach provided by ROI\_PAC (Rosen et al. 2004), which determined the maximal correlation between master and slave images, for a pre-set window size. The distance between the peaks of 2D cross-correlation in two images corresponds to the extent of the glacier motion. Owing to the image normalization, differently illuminated images can be compared (Heid and Käab 2012). Such processing allows calculating the LOS and azimuthal direction displacements.

For optical images, we processed offset tracking using the co-registration of optically sensed images and correlation (COSI-Corr) software (Leprince et al. 2007; Ayoub et al. 2009), which yields reliably stable results for monitoring of the glacier displacement (Heid and Käab 2012). COSI-Corr processed cross-correlations in the Fourier domain, along with the iterated Gaussian weighted least squares, to avoid outliers within the windows, which ensured robustness of the resultant displacement in the images’ x and y directions.

For both SAR and optical images, pairs of images were also organized in a continuous chronological order (i.e., in the AB, BC, CD manner), to preserve the shortest temporal baseline and avoid large landscape deformation. Based on the findings in Tsai et al. (2018), the window size was set to 128 pixels by 128 pixels to detect the tracked features and displacement details.

### 3.3 3D Decomposition

Because the movement vectors derived using different techniques are in different directions, which are decided by the sensing incidence angle ( $\theta$ ) and satellite heading angle ( $\varphi$ ) (the geometry is shown in Fig. 3), it is difficult to compare them directly. Fortunately, because all vectors can be treated as projections of local 3D displacements in different directions, they can be represented using the following equations (Hanssen 2001):

$$\begin{bmatrix} d_{\text{Range(SAR)}} \\ d_{\text{Azimuth(SAR)}} \\ d_{\text{X(Nadir optical)}} \\ d_{\text{Y(Nadir optical)}} \end{bmatrix} = \begin{bmatrix} \sin \theta \cos \varphi & -\sin \theta \sin \varphi & -\cos \theta \\ \sin \varphi & \cos \varphi & 0 \\ \cos \varphi & -\sin \varphi & 0 \\ \sin \varphi & \cos \varphi & 0 \end{bmatrix} \begin{bmatrix} E \\ N \\ U \end{bmatrix} \quad (1)$$

where E, N, U are the eastward, northward, and upward displacements;  $d_{\text{Range(SAR)}}$  and  $d_{\text{Azimuth(SAR)}}$  are the SAR images’ offset tracking vectors; and  $d_{\text{Easting(Nadir optical)}}$  and  $d_{\text{Northing(Nadir optical)}}$  are the optical images’ offset tracking vectors. Using this equation, the Cartesian displacement (ENU) can be extracted from the data obtained using different techniques, allowing the validation and application of the method.

## 4. PROCESSING OF RESULTS AND VALIDATION

### 4.1 Movement in Summertime (SAR PO + Optical PO) 3D Decomposition

To derive the 3D displacement during summertime, both SAR and optical images acquired during July (Table 3) were independently processed using the offset tracking approach, to estimate the movement of the glacier surface in four different directions. The images had close acquisition time, temporal interval, and spatial resolution, ensuring that the resultant displacements were comparable. It should be noted that due to the 16 days revisiting time of Landsat-8, we selected 12 days Sentinel-1A pair to process PO but not utilizing both Sentinel-1A and -1B. As 6 days interval would be too short to compare with optical images while 18 days interval would largely degrade the PO results.

For further data fusion and 3D decomposition processing, the points of displacements were first interpolated, cropped to the same boundary, and converted to meter/day units. Moreover, to ensure the reliability of the observed displacement, we classified the results of SAR and optical PO into lower and higher reliable parts individually based on their quantile value of PO Signal-to-Noise-Rate (SNR) value which was generated using COSI-Corr and ROI\_PAC indicating the quality of correlation (Leprince et al. 2007; Tsai et al. 2018). The SNR value ranges from 0 to 1 representing no and perfect correlation, respectively. It is a valuable indicator for evaluating the confidence of the resultant displacement and was therefore utilized in many studies (Kraaijenbrink et al. 2016; Peppia et al. 2017; Rathje et al. 2017). In this paper, the reliability masks of SAR and optical images were respectively constructed taking SNR pixels of all-time 50% quantile (Figs. 4a and b) and then merged into the final PO reliability mask as shown in Fig. 4c.

Comparison of the SAR LOS and optical Easting directions (Fig. 5a) reveals similar magnitudes and patterns. The deformation was observed in five termini and upstream of the glaciers Isunnguata Sermia, Russell, and unnamed one. Similar flow directions were also noted for the SAR azimuthal and optical Northing directions over the crossing branch of the glaciers Ørkendalen and Isorlersuup. Those simple cross-comparisons suggested the similarity of the offset tracking of both SAR and optical images for detection of supraglacial velocity although their sensing angles are different. Additionally, by comparing the masked area

of two PO results, it is clear that the noise-contaminated part of SAR PO extends deeper from inland part to terminus region, which inevitably decreases the coverage of analyzable part. We considered it is because the speckles of SAR images are more complicated than optical images as they are caused by nearly random constructive and destructive interferences generated from surface features. However, it is worth noting that this issue is not problematic for wintertime InSAR time-series as we utilized phase information of SAR and stacking approach to mitigate noise for wintertime (referred to Fig. 2).

Based on four observed motion vectors, we then calculated the ENU displacements as shown in Fig. 5b. To avoid the risk may mislead the resultant ENU displacement, only the reliable part in both SAR and optical PO results is further analyzed, i.e., using the final mask shown in Fig. 4c. The resultant ENU displacement reveals a clear westward and downward velocity of the entire ice sheet, especially at the north-south crossing of the glaciers Ørkendalen and Isorlersuup (Fig. 5b) with the maximum magnitude around  $0.5 \text{ m day}^{-1}$ . This observation agrees with previous studies spatially and quantitatively (Rignot and Mouginot 2012;

Fitzpatrick et al. 2013; Morlighem et al. 2013). However, the inner ablation zone is nearly all masked out due to large noise. An interesting discovery is several clear vertical surface lowering (white dotted circles in U in Fig. 5b), which are almost located in the marginal termini region.

#### 4.2 Movement in Wintertime (InSAR Time Series)

For wintertime data, the InSAR time series data, consisting of Sentinel-1A and -1B, were employed to create a InSAR time-series velocity stack with the shortest interval of 6 days as the interchangeability was confirmed by Geudtner et al. (2018). Using the time series interpolation, a cumulative displacement in the LOS direction was calculated. Although we employed the shortest temporal baseline method to build the InSAR stack, the quick landscape changing of glacier would inevitably decrease the coherence of D-InSAR, which is a critical index to evaluate the reliability of unwrapped interferogram and final displacement. Hence, it would be necessary to first investigate the temporal coherence stability. However, as the total correlation value generally includes not only temporal but thermal as well as spatial components

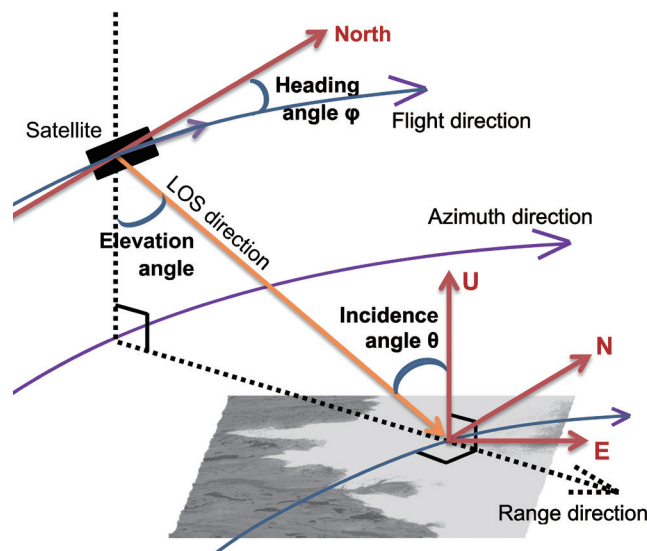


Fig. 3. Imaging geometry and the solved displacements in eastward (E), northward (N), and upward (U) directions through 3D decomposition.

Table 3. Detailed information of the Landsat-8 and Sentinel-1 images used for summertime movement analysis.

Image type/sensor	Optical Landsat-8	SAR Sentinel-1
Acquisition date	July 10 to July 26	July 16 to July 28
Temporal baseline (days)	16	12
Spatial resolution (meter)	15	$5 \times 20$
Technique	Offset-tracking	Offset-tracking
Displacement	2D (Easting, Northing)	2D (Range, Azimuth)

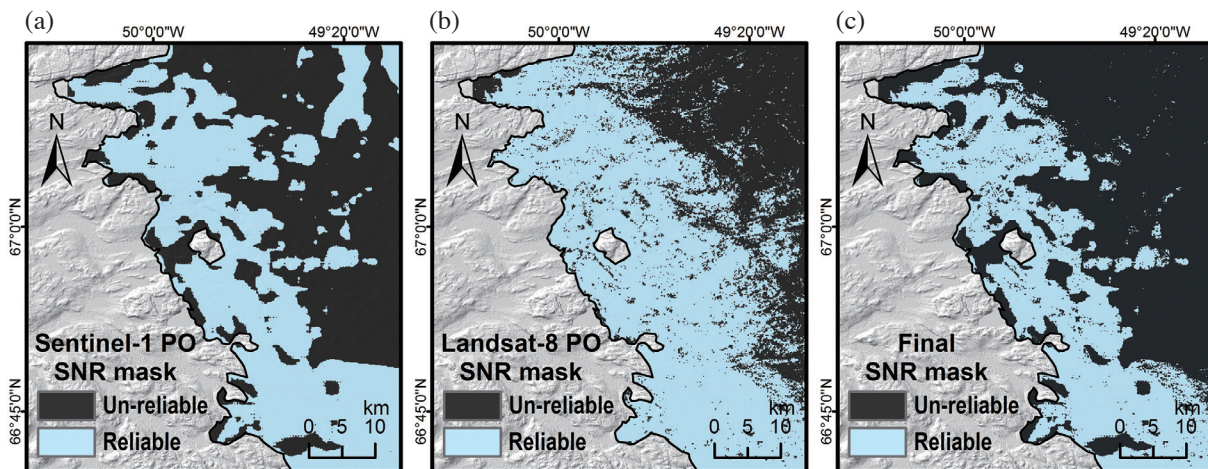


Fig. 4. The signal-to-noise (SNR) value masks of PO of (a) Sentinel-1 SAR and (b) Landsat-8 optical results. The reliabilities of observations are classified using the quantile value of SNR. (c) is the final mask with only region classified reliable in both (a) and (b).

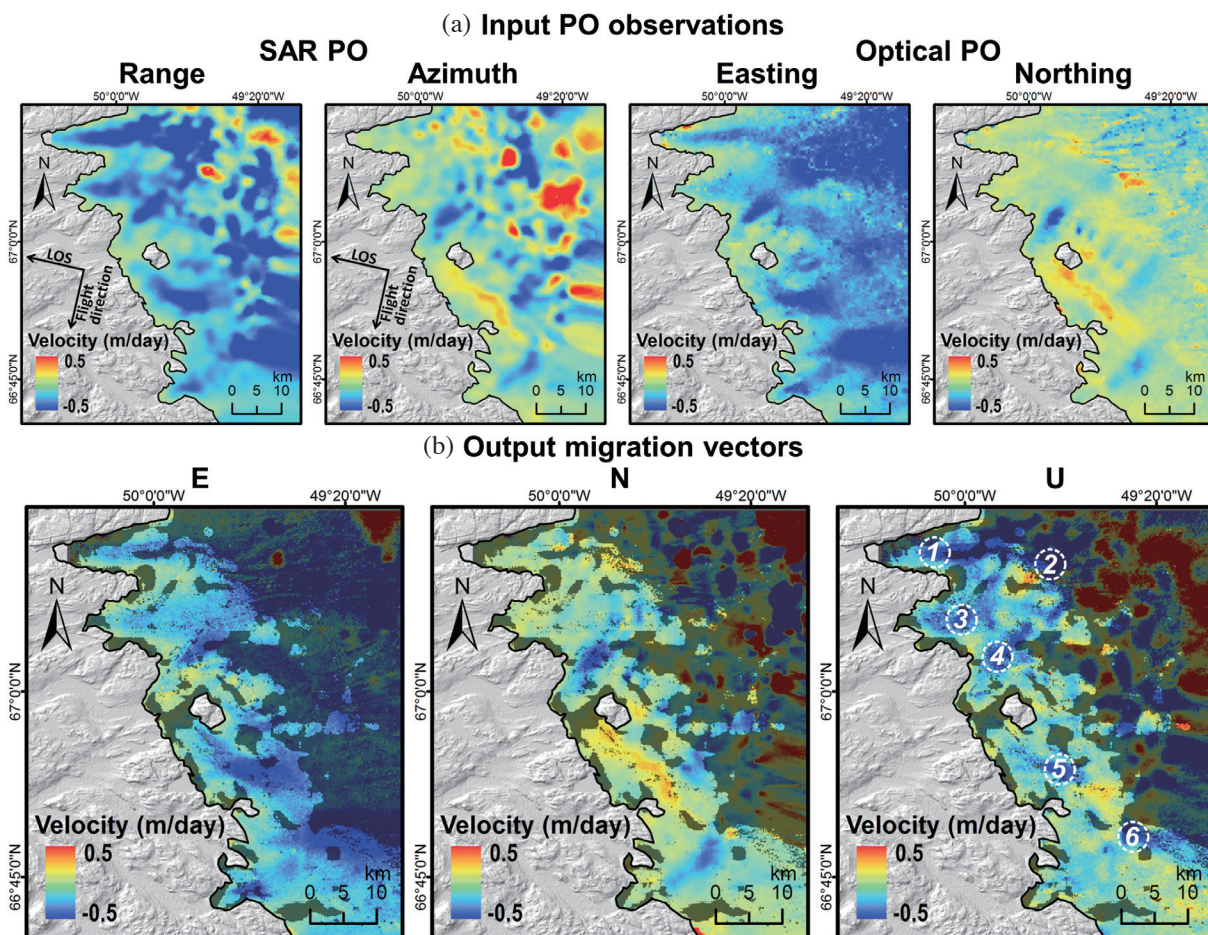


Fig. 5. Summertime 3D decomposition results, where (a) is the input PO observations and (b) is the output velocity vectors. The semi-transparent black mask represents the unreliable region calculated from Fig. 4. The white dotted circles outlined in U-direction in (b) indicate the location of obvious local vertical lowering regions (see Fig. 14 for identifying the numbered sites).

(Zebker and Villasenor 1992), we need to calculate later two to infer the needed temporal coherence.

Because Sentinel-1 TOPS sensing behaves high quality of SNR value, the thermal decorrelation can be presumed neglectable; and the spatial correlation can be modeled with (Zebker and Villasenor 1992):

$$\rho_{spatial} = 1 - \frac{2|B|R_y \cos^2 \theta}{\lambda r} \quad (2)$$

where  $B$  is the perpendicular baseline of InSAR pair,  $R_y$  is the SAR resolution in range direction,  $\theta$  is the incidence angle,  $\lambda$  is the SAR wavelength, and  $r$  is the distance between SAR sensor and the ground target. Excepting the fixed range resolution and wavelength, the perpendicular baselines of each pair were calculated as listed in Table 2, and the location of satellite at sensing time were extracted from the Sentinel-1 precise orbit ephemerides.

After calculation, the spatial coherence of each pixel of each pair can be estimated. Following we divided the original InSAR coherence by calculated spatial coherence to infer interested temporal coherence map of each pair (Fig. A1 in Appendix), and further calculated the average and standard deviation of temporal coherence of each pixel as shown in Fig. 6. It makes sense to use them as the reliability metrics of InSAR observations as the large dispersion of phase coherence is normally considered the loss of reliable InSAR signal in observational time domain.

The average temporal coherence over bedrock regions is higher than glacier regions around 0.15, suggesting the reliability of bedrock part is higher. However, it is also noted that even in the glacier region still have coherence value around 0.3 to 0.45, which is actually above conventional D-InSAR unwrapping threshold and thus is high enough to trust its final displacement. Furthermore, by checking the standard deviation of temporal coherence, the glacier region reveals compatible or even lower variances to stable bedrock part. It implied that although the glacier region shows relative lower surface coherence due to quick landscape changing and motion, it remains the stable variation over time. The reliability of InSAR time-series displacement over glacier part was therefore proved.

The resultant mean extension velocity in LOS direction derived from the whole InSAR stack is shown in Fig. 7 with the highest speed around  $-0.1 \text{ m day}^{-1}$ . The maximal cumulative displacement of up to 7 m was observed in five termini and their upstream areas, showing spatial similarity with the summertime results (Fig. 5b). However, the mechanism causing deformation of two seasons are different as comprehensively following discussed in section 5.2. Also, as the InSAR can only sense in LOS direction, which implied that huge displacement includes not only vertical surface lowering but horizontal movement components projected to LOS

angle. To analyze the spatial and temporal velocity trends, we plotted total deformations for eight local main deformation points, and the resulting plot revealed that velocity trends are nearly the same across the whole area.

### 4.3 Validation Using ESA CCI Results

To validate our summertime and wintertime results, the velocity product of the ESA CCI was utilized. As mentioned in section 2.2.2, although it is the most suitable ground truth data available for validation, its 500 m resolution and annual static average might cause uncertainty of reliability. However, the overall spatial pattern and magnitude of the Russell glacier velocity should still be representative and comparable.

Firstly, the wintertime cumulative displacement is validated. Nevertheless, as our InSAR time-series results is in LOS direction which cannot be directly compared with the ESA CCI velocity product's ENU direction, we projected the ESA velocity to Sentinel-1's sensing angle using formula 1 used in 3D decomposition, the LOS direction extension rate projected result is shown in Fig. 8.

In general, the spatial patterns were similar across the ESA CCI product and our wintertime InSAR time series displacement, showing clear deformation in the termini and upstream areas, and the crossing direction of the glaciers Ørkendalen and Isorlersuup. However, owing to the higher spatial resolution of our InSAR map, a more detailed deformation anomaly was observed. On the other hand, the magnitude of the ESA annual averaged velocity was found to be around twice larger than our observations, since the velocity that was measured here only accounted for wintertime (season with relatively slow flowing velocity), which is similar to the conclusions of studies conducted before 2010 (Van de Wal et al. 2008; Pritchard et al. 2009; Joughin et al. 2010).

To examine the spatial distribution of the velocity magnitude, profiles along the flowlines were drawn and shown in Fig. 9. The flowlines of Russel glacier were from previous studies (Fitzpatrick et al. 2013; Morlighem et al. 2013), and our wintertime InSAR results (Fig. 8a) also demonstrated similar patterns as drawn as the dashed black lines in Fig. 8. Comparable trends were observed for all five termini excepting the terminus part of Ørkendalen glacier (flowline 3). There are several reasons causing that mismatch, including: (1) the highest velocity in LOS direction over that part among the whole studying area (as shown in the ESA CCI product in Fig. 8b). This would cause the significant decorrelation for D-InSAR and consequently the failure of detection of true displacement. This assumption can be confirmed as that part does show much lower average temporal coherence as shown in Fig. 6; (2) as ESA CCI product is annual average velocity, not only the magnitude but pattern of glacier velocity in wintertime would be different especially in terminus region due to less melting water-lead acceleration

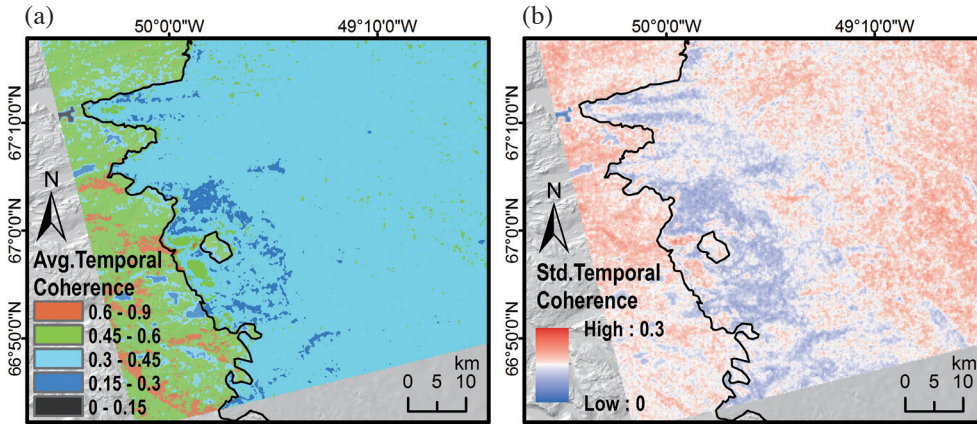


Fig. 6. Temporal coherence of InSAR time-series stack, where (a) is average and (b) is standard deviation value. Note the glacier region shows sufficient enough average coherence value (0.3 - 0.45) and with standard deviation value lower than bedrock region, suggesting its reliability.

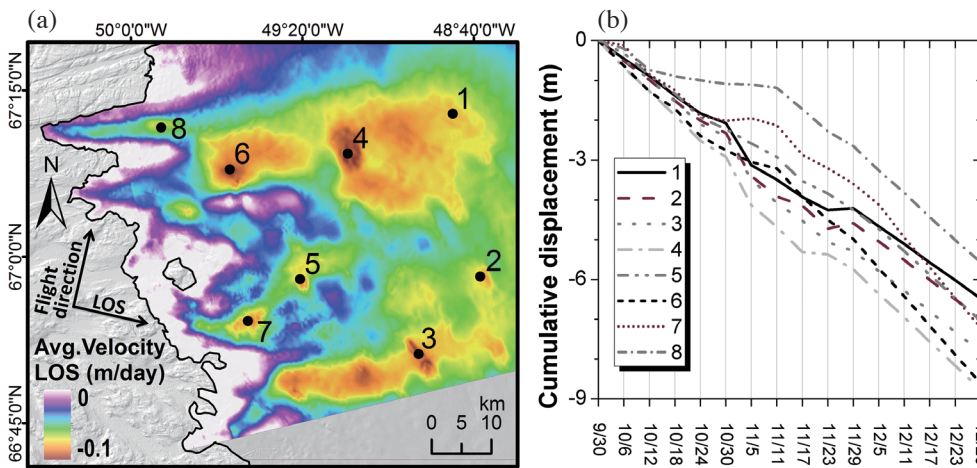


Fig. 7. Results of the wintertime InSAR time series analysis. The derived spatial pattern of extension velocity in LOS direction is shown in (a) while the total deformation for eight local main lowering points is illustrated in (b). A lowering velocity with similar magnitude was observed in all examination points with cumulative deformation up to 7 - 9 m.

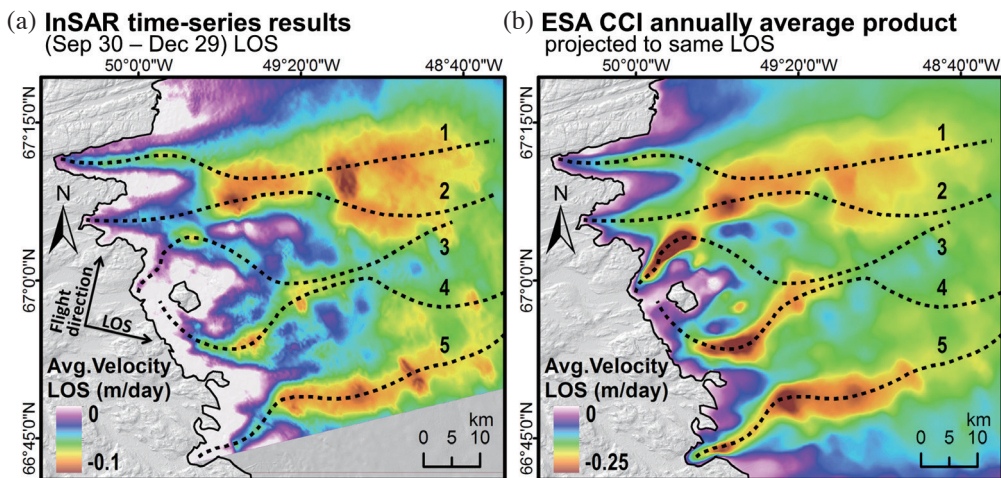


Fig. 8. Validation of InSAR time series (a) using the ESA CCI annually average product projected into LOS direction of our InSAR observations (b). The InSAR time series result shows high agreement with the ESA CCI product. Detailed local displacement is also observed in (a) due to the high spatial resolution of our InSAR displacement map. The flowline of each glacier is illustrated with black dashed line.

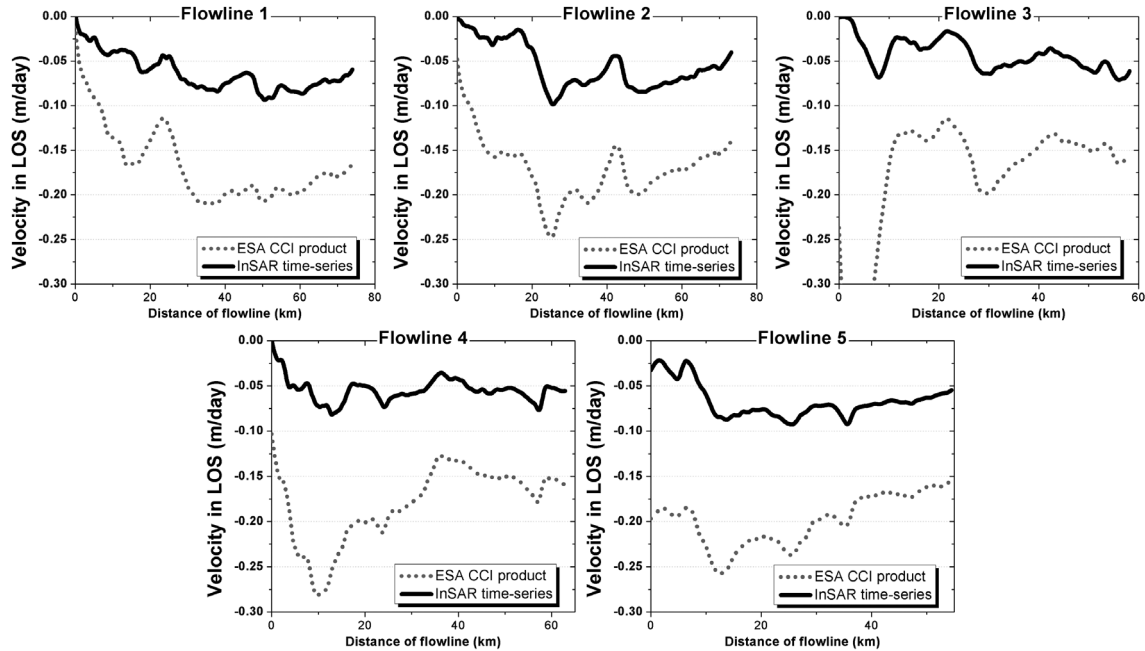


Fig. 9. Validation of InSAR time series using projected ESA CCI annually average product over each glacier's flowline. The flowline distance calculates from terminus to inland. Owing to the seasonal difference of study period, the overall magnitude of ESA CCI product is around twice to threefold than our InSAR observations. However, the high spatial agreement between our InSAR time-series result with ESA CCI product is clearly observed in all five termini.

(following discussed in section 5.2); (3) in technical aspect, it might be stem from the side effect of de-ramping routine of GIANt which misjudged the parallel deformation pattern of terminus as targeted long wavelength ionospheric error which happened frequently in high latitude regions for C-band Sentinel-1 images (Brcic et al. 2011; Gomba et al. 2017). In addition to this mis-match part, the overall magnitude of ESA CCI product is around twice to threefold than our InSAR observations as shown in Fig. 9. This value fits the seasonal differences of glacier flowing speed as our InSAR time-series analysis only cover wintertime but ESA CCI product is annual average as mentioned in section 2.2.2. There also might be certain influence on the different LOS migration speed by the applications of de-ramping routines, which is essential to reduce long wavelength phase noise such as orbital error as described in section 3.1.

The summertime 3D decomposed local ENU results were also validated based on the ESA CCI velocity product. The same flowlines of each terminus were used for profiling and the trends of spatial displacement were shown in Fig. 10. Overall, the comparable trends are revealed in all five termini especially in the Easting direction, while in both the Northing and vertical directions shown much poorer similarity. We considered it is because the surface slope of studying land-terminating glaciers is in facing the seashore, i.e., west-facing as shown in Fig. 1, the deformation toward the west is hence nearly relatively constant even in quick moving summertime. In contrast, the motion in the North-

ing and vertical directions would be more adapt to the local landscape which is easily altered by surface melting, snow accumulation as well as surface runoff causing by higher temperature and more precipitation during summertime as discussed in section 5.2. This driven force difference may explain the obvious mismatches of the Northing motion in both flowline 2 and 3, which spatial location is near the sharp turning points of the glaciers Ørkendalen and Isorler-suup. It is worthwhile noting that the motion in the vertical direction is always bigger than ESA CCI which is annual mean speed. It represents that our PO results well depict the basal melting in summer season which agrees with De Fleurian et al. (2016). However, the poor azimuth resolution of Sentinel-1 compared to range, i.e., 5 - 20 m, can induce some distortions mainly in the northward direction as discussed in Sánchez-Gómez and Navarro (2017). Thus, the large discrepancies in the Northing direction may include such components.

## 5. DISCUSSION

Since the glacier movement has been identified in depth, we conducted further interpretation based on our remote sensing observations. In particular, we are interested in exploring the relationship between surface velocity over glacier and driving factors such as bedrock altitude and climate conditions. To identify the clues of ice dynamics, not only the remote sensing observations but also a complemented

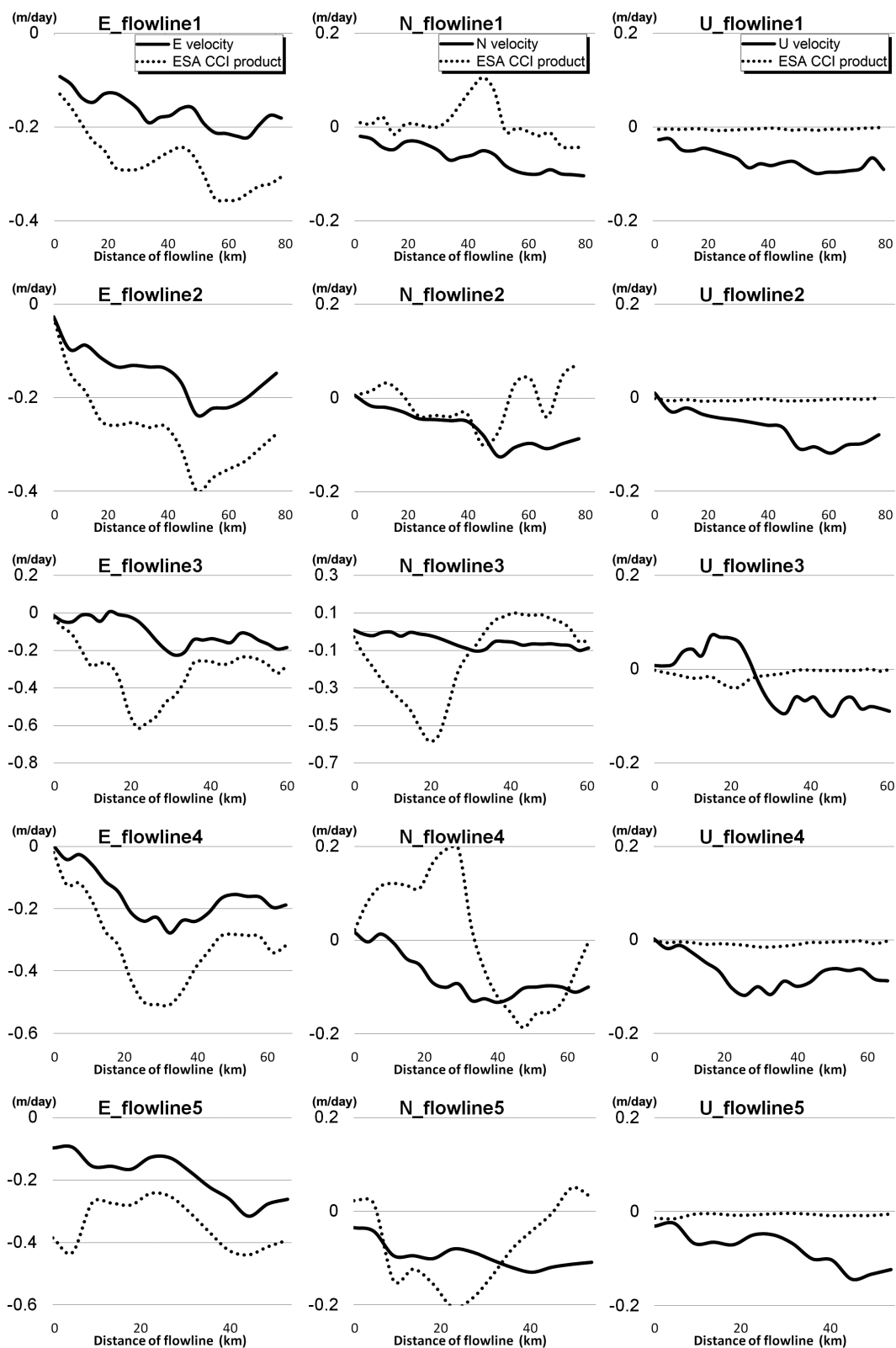


Fig. 10. Validation of 3D displacement through the comparison between ESA CCI (black dotted curve) and summertime ENU displacement (black solid curve) over each glacier flowline. The flowline distance calculates from terminus to inland. The negative value of Easting and Northing indicates Westing and Southing respectively.

numerical model and time series information of weather forecasting were applied.

### 5.1 Basal Condition Estimation by Numerical Ice Sheet Model

Based on our remotely sensing observations, we could identify the spatial pattern of glacial surface motion; however, it is not sufficient to understand the friction condition of ice/bedrock interface which is a strong predictor of glacial dynamics. Thus, we employed the ice sheet model (ISM) and further explored the basal conditions in line with our remote sensing observation.

The basal condition is extracted through the ISM inversion process, including four steps: (1) importing the surface velocity, (2) setting up the ice flow equations, (3) analyzing the boundary conditions, and (4) inverting the basal friction. First, to analyze and compare seasonal differences, we considered the ISM within summertime and wintertime velocities, separately. Then, a 3D higher-order (HO) model (Blatter 1995; Pattyn 2003) was employed, which takes into account the vertical shear together with the membrane stress of each layer, but ignores the bridging effect of the ice sheet. Because the Russell glacier is a land-terminating glacier, which neither overlaps with the sea nor features floating ice, and because the atmospheric pressure over the ice sheet surface can be ignored (Gagliardini et al. 2013), the ice/bedrock boundary is the only interface that should be analyzed. In ISM, the drag friction condition of grounded ice normally be defined as the following linear relationship (MacAyeal 1989, 1992):

$$\tau = -\alpha^2 v \quad (3)$$

where  $v$  is the horizontal velocity tangential to the ice/bedrock interface,  $\alpha$  is the friction coefficient, and  $\tau$  is the shear stress or basal traction. Then, the variation inversion is employed to iteratively solve the cost function for minimization of the discrepancy between the input observed velocity and output modeled velocity. Using the four steps described above, the basal friction can be obtained given the observed surface velocity.

To estimate the basal friction condition, we processed the ISM with the ice sheet system model (ISSM) (Morlighem et al. 2010; Larour et al. 2012), which is a powerful and well-maintained open-source modelling platform. The input raster, including the surface velocities described in sections 4.1 and 4.2 for summertime and wintertime, respectively, the bedrock height and the ice thickness derived from the NASA OIB and the air temperature data of SeaRISE, were all interpolated into the anisotropic mesh with the resolution of 1 km, and extruded to ten layers to form an initial glacier mesh. Regarding other parameters,

we used the default value of ISSM, such as initial uniform friction coefficient and initial temperature field change were set to 10 and 0 K, respectively.

To firstly test the reliability of the ISM, we examined the similarity between input (observed) and output (modeled) velocities. The results show a comparable match for the velocity in Easting and Northing directions, in terms of both the pattern and magnitude, as shown in Fig. 11. It indicates the modelling process reaches convergence and hence guarantees the reliability of the modeled friction coefficient. In addition, the magnitude and the main moving area between two seasons were noted. First, the speed during summertime is about three times higher than the speed during wintertime.

Because the convergence of the modelling process is confirmed, the quality and accuracy of modeled basal friction, can be ensured. Comparing the modeled friction of the ice/bedrock interface with observed surface velocity in Fig. 12, it is clear that a lower friction occurs in a faster moving area, which agrees with the results of previous studies (Morlighem et al. 2013; Larour et al. 2014) as well as our observations. Because the magnitude of the surface movement is much larger in summertime, the basal friction is naturally lower. Together with the wintertime shrinking of the surface moving area, the regions that exhibited lower basal friction were also found to retreat inland. Additionally, while the surface velocity seems generally smooth, the basal friction value show more heterogeneous pattern beneath which suggests the complex ice/bedrock interface condition. In addition, those outcomes by numerical ice sheet model compared to the remote sensing observation ensured the strong basal friction over the frontal part of glacier, which imply the correlation between bedrock morphology and surface velocity.

### 5.2 Glacial Dynamics by Remote Sensing Observations and Climate Data Set

Based on the theories of cryo-hydrologic system (CHS) (Thomsen et al. 1988; Hanna et al. 2008; Van de Wal et al. 2008; Cuffey and Paterson 2010) and thermal-viscous system collapse (Robin 1976; Colgan et al. 2015), it is understood that ice movement is largely dominant by melting water and ice mass pressure. Through the observations of the five glaciers (Fig. 7), bedrock height and the subglacial topography derived from the NASA OIB data (Fig. 13), we found that five termini shown in Fig. 1 all represent subglacial channelized trough systems, which are also parallel to the ice flow direction and exhibit a strong negative correlation between the depth of channel and the ice flow velocity (Lindbäck and Pettersson 2015). In particular, the correlation map between wintertime InSAR LOS velocity and bedrock altitude shown in Fig. 13c implied the possibility that the sub-glacier topography and ice thickness

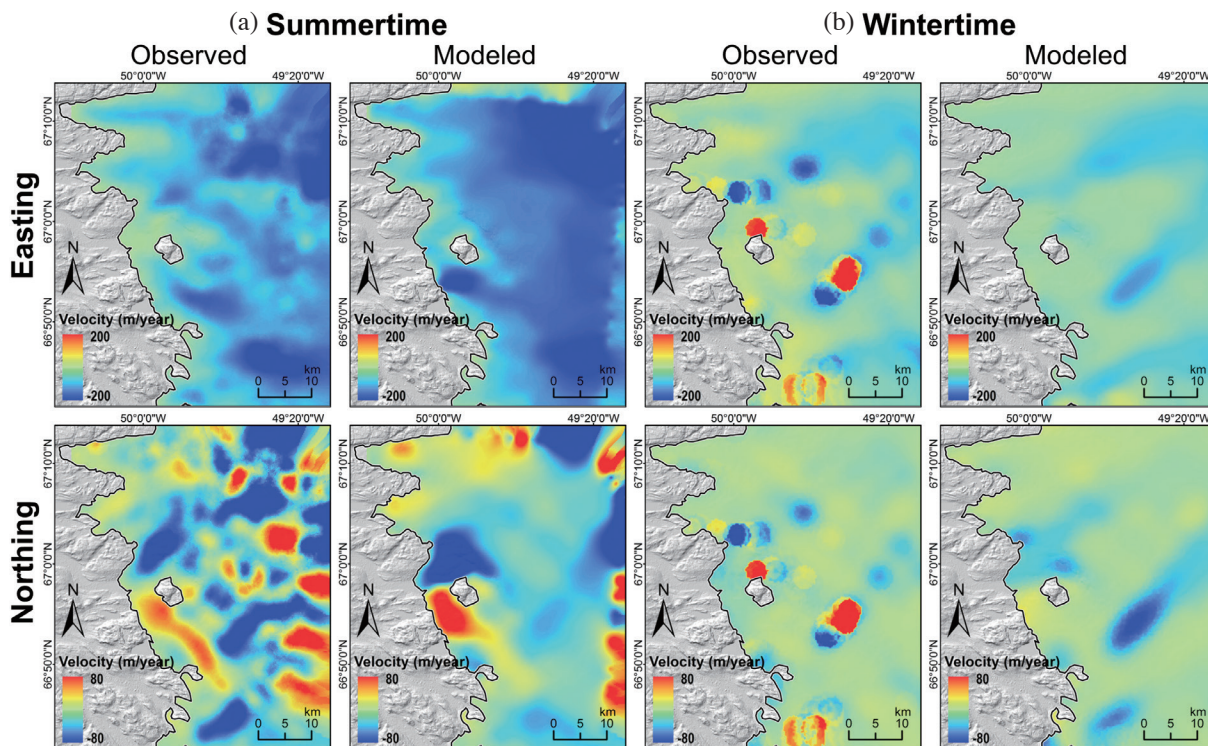


Fig. 11. Results of the numerical ice sheet model (ISM) of summertime (a) and wintertime (b). A high agreement between observed and modeled velocities in each direction of two seasons is observed. Note that the unit of velocity is presented in m/year for consistency of the requirement of ISM.

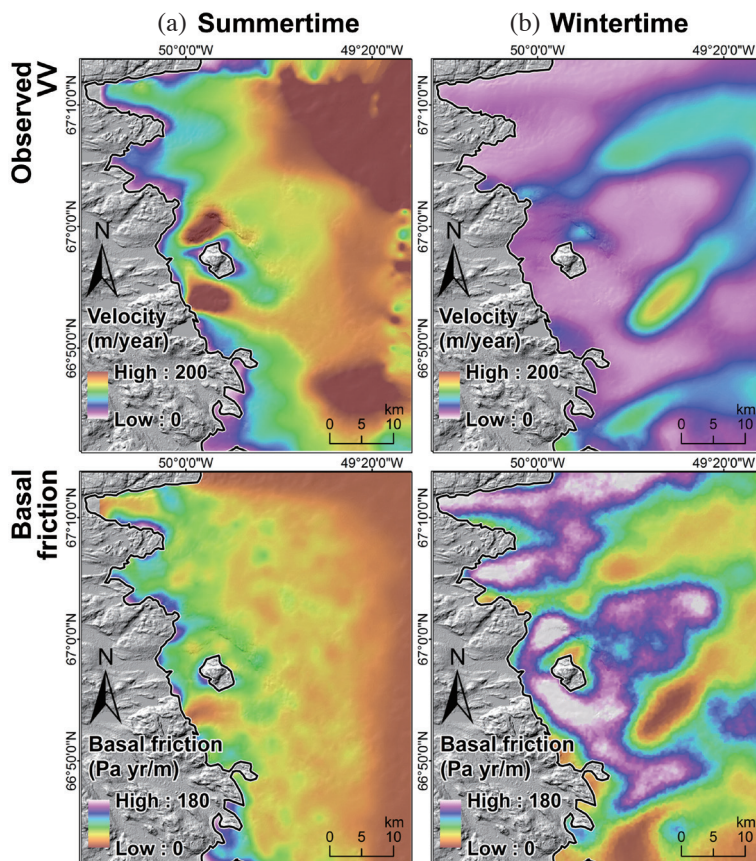


Fig. 12. Results of the numerical ice sheet model of summertime (a) and wintertime (b). The observed VV is the total horizontal velocity, i.e., square root of easting and northing velocity. The smaller velocity and higher basal friction are clearly represented in results derived in summertime.

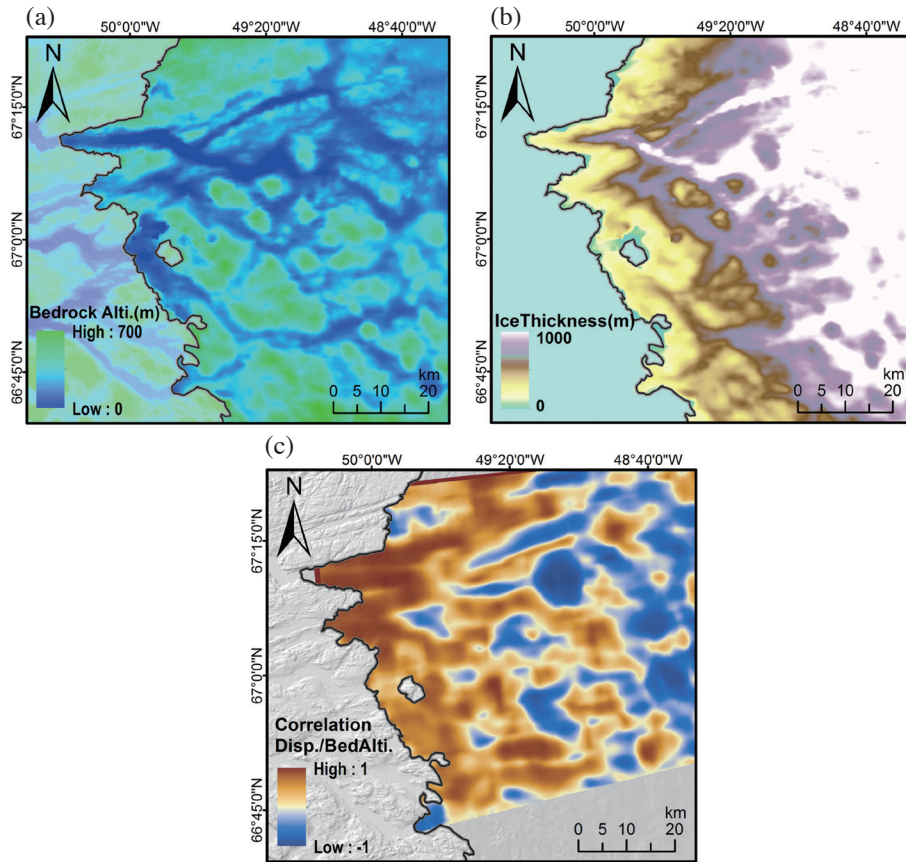


Fig. 13. Bedrock height (a) and ice thickness (b) extracted from the NASA OIB data. (c) Spatial correlation between observed wintertime deformation and bedrock altitude. The five termini shown in Fig. 1 all demonstrate deep troughs structures in (a) and thick ice in (b) as well as high surface velocity in Fig. 8a. Strong correlation between InSAR deformation and bedrock altitude over the termini frontal part of glacier is shown in (c).

dominantly control the dynamics of ice sheet at least over the termini frontal parts.

Furthermore, our 3D decomposition results revealed the supraglacial features which may be related to the vertical lowering anomaly over summertime displacement as shown in Fig. 14a. We overlapped the digitized surface line-shaped features (black curves) from summertime Sentinel-2 image with vertical lowering regions (white dotted circles). All surface lowering regions were also found with clear or snow-covered crevasses features as shown in Fig. 14b. The quantitative evaluations using signal-to-noise mask shown in Fig. 5 proved five of them are located within quite secured observations. It should be noted that the modeled basal friction in Fig. 12 does not have similar feature to those summertime lowering regions. Thus, the origin of such anomaly is not likely related to the bedrock morphology. To examine the surface lowering velocities over anomalies, we calculated the average lowering speed based of each obvious deformation zones (white dotted circles in U in Fig. 5) as shown Fig. 14c. All five surface lowering zones show velocity around  $-0.4 \text{ m day}^{-1}$  in studying summertime period and the strong downward deformation over area 2. Therefore, we proposed those surface lowering regions can be better ex-

plained by genuine displacement possibly involved with water transporting conduits rather than the observation noise.

Also, by comparing the meteorological data recorded by the automatic weather station (AWS) located in the Kangerlussaq close-by the Russell glacier, we can reasonably infer that the difference between velocities stems from the impact of temperature and rain events, as shown in Fig. 15. Because the precipitation runoff has higher temperature compared with glacial meltwater, and because it would drain into the interior and bottom of the ice sheet, both the thermal transfer and lubrication effects would largely accelerate the ice sheet movement. In addition, the higher temperature would heat up the glacier, consequently yielding more englacial meltwater, and would also increase the water pressure in the subglacial channel, which would decrease the friction at the ice/bedrock interface. Because summertime is characterized by higher temperatures and larger amounts of precipitation, the speed of the glacier would undoubtedly be higher in summertime.

## 6. CONCLUSIONS AND FUTURE WORK

To respond to the increasing interest in glacial velocity

especially over the GrIS which correlates with the worldwide climate change, and to fulfil the requirements of accurate interpretation based on continuously derived spaceborne image data, we proposed a monitoring strategy to identify the major characteristics of glacial velocity in different seasons by combining short-term remote sensing observations and validation using external data. Firstly, to define precise glacial velocity over the land-terminating Russell glacier area located in southwestern Greenland, offset tracking analysis using Landsat-8 optical and Sentinel-1 SAR images acquired during 2016 was conducted for estimating the local ENU displacement. The result was then fused to decompose 3D deformation vectors. The summertime/wintertime

3D velocity measurements of the Russell glacier together with the InSAR LOS displacement were then validated by comparison to the global Greenland displacement data in the ESA CCI and the quality metrics such as signal-to-noise of offset tracking and InSAR phase coherences. Although some remote sensing observations were contaminated by noise, it was demonstrated that the extracted ice sheet velocities over the target glacier were reliable. The numerical ice sheet model employing glacial velocity components yielded useful information about the heterogeneous basal friction as well as its seasonal difference. By overlapping vertical displacements for 3D glacial velocities, modeled basal frictions and a few vertical lowering regions, which might be involved with

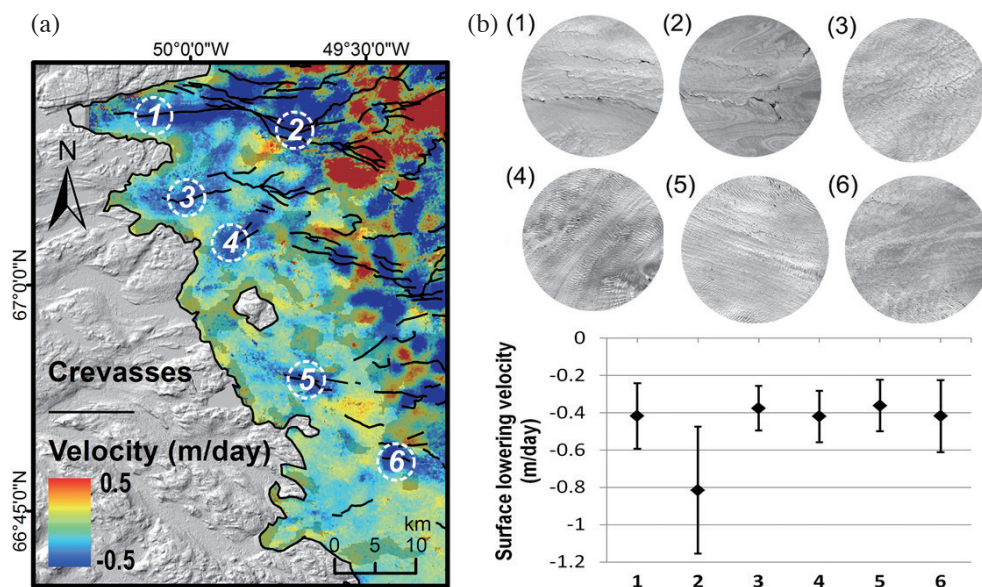


Fig. 14. Vertical surface lowering regions and the corresponding supraglacial features over summertime U deformation (a) and vertical subsidence regions (b) observed by Sentinel-2 image. The snow-covered crevasses/moulins features are clearly represented in all 6 vertical subsidence regions. Surface lowering velocity of each terminus's obvious deformation zone (white dotted circles in U in Fig. 5) is presented in (c).

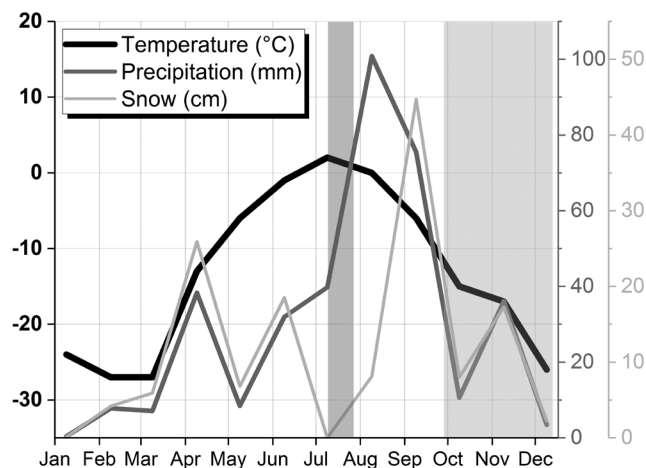


Fig. 15. Weather data for study area during 2016. The seasonal coverage of the data applied this study is represented by grey box (summer) and light grey box (winter). The quick glacier moving velocity estimated in summertime is associated with annually maximum temperature and precipitation.

potential supraglacial activities, were identified.

Based on the results of our studies, we conclude that the effective integration of remote sensing observations with models and weather observations can provide valuable clues about glacial velocity, even though the temporal coverage, number, and quality of remote sensing observations might be not sufficient. At the end, this study proved the reliability of PO method, the ice sheet modelling, short temporal baseline InSAR time-series observations employing Sentinel-1 image data fusion approach of multi-sensor data and numerical models over glacial surface. Considering all of the difficulties associated with remote sensing and ground measurements, the approaches we employed in this study can be applicable over many GrIS, Antarctic, and inland glacial areas because the approach enable to trace the seasonable ice sheet change even with limited number of spaceborne observations. In the future, we are planning to apply this approaches to target areas with more complicated environments; for instance, outlet glaciers affected by tidal effects. The results of those future studies can likely be validated using higher spatial and temporal resolution spaceborne images, for tracking glacial displacements in more details and for conquering the baseline limitation of the InSAR approach. In addition, the cross-comparison and fusion of data acquired by newly deployed sensors, such as spaceborne altimeters (including ICESat-2) and consecutive ALOS-2 PRISM-2 stereo image acquisitions which enable to make quantitative surface velocity tracing, will be attempted. Especially it will be very interesting to consider the potential of L-band SAR, which may be more robust with a long-term baseline and can be fused with C/X band SAR and optical image outputs.

**Acknowledgements** This work has been supported by the Korean ministry of Land, Infrastructure and Transport (Greenland Mapping Project) and University of Seoul. The authors thank the Greenland local government and ASIAQ Greenland Survey for their useful advices and supports.

## REFERENCES

- Agram, P. S., R. Jolivet, B. Riel, Y. N. Lin, M. Simons, E. Hetland, M. P. Doin, and C. Lasserre, 2013: New radar interferometric time series analysis toolbox released. *Eos, Trans. AGU*, **94**, 69-70, doi: 10.1002/2013eo070001. [[Link](#)]
- Arslan, A. N., H. Wang, J. Pulliainen, and M. Hallikainen, 2001: Effective permittivity of wet snow using strong fluctuation theory. *Progress in Electromagnetics Research*, **31**, 273-290, doi: 10.2528/pier00071709. [[Link](#)]
- Ayoub, F., S. Leprince, and J. P. Avouac, 2009: Co-registration and correlation of aerial photographs for ground deformation measurements. *ISPRS J. Photogram. Rem. Sens.*, **64**, 551-560, doi: 10.1016/j.isprsjprs.2009.03.005. [[Link](#)]
- Baltsavias, E. P., E. Favey, A. Bauder, H. Bosch, and M. Pateraki, 2001: Digital surface modelling by airborne laser scanning and digital photogrammetry for glacier monitoring. *Photogramm. Rec.*, **17**, 243-273, doi: 10.1111/0031-868x.00182. [[Link](#)]
- Bamber, J. L., J. A. Griggs, R. T. W. L. Hurkmans, J. A. Dowdeswell, S. P. Gogineni, I. Howat, J. Mouginot, J. Paden, S. Palmer, E. Rignot, and D. Steinhage, 2013: A new bed elevation dataset for Greenland. *The Cryosphere*, **7**, 499-510, doi: 10.5194/tc-7-499-2013. [[Link](#)]
- Baran, I., M. Stewart, and S. Claessens, 2005: A new functional model for determining minimum and maximum detectable deformation gradient resolved by satellite radar interferometry. *IEEE Trans. Geosci. Remote Sensing*, **43**, 675-682, doi: 10.1109/tgrs.2004.843187. [[Link](#)]
- Barrand, N. E., T. Murray, T. D. James, S. L. Barr, and J. P. Mills, 2009: Optimizing photogrammetric DEMs for glacier volume change assessment using laser-scanning derived ground-control points. *J. Glaciol.*, **55**, 106-116, doi: 10.3189/002214309788609001. [[Link](#)]
- Bartholomew, I. D., P. Nienow, D. Mair, A. Hubbard, M. A. King, and A. Sole, 2010: Seasonal evolution of subglacial drainage and acceleration in a Greenland outlet glacier. *Nat. Geosci.*, **3**, 408-411, doi: 10.1038/ngeo863. [[Link](#)]
- Bartholomew, I. D., P. Nienow, A. Sole, D. Mair, T. Cowton, M. A. King, and S. Palmer, 2011: Seasonal variations in Greenland Ice Sheet motion: Inland extent and behaviour at higher elevations. *Earth Planet. Sci. Lett.*, **307**, 271-278, doi: 10.1016/j.epsl.2011.04.014. [[Link](#)]
- Biggs, J., T. Wright, Z. Lu, and B. Parsons, 2007: Multi-interferogram method for measuring interseismic deformation: Denali Fault, Alaska. *Geophys. J. Int.*, **170**, 1165-1179, doi: 10.1111/j.1365-246x.2007.03415.x. [[Link](#)]
- Bindschadler, R. A., S. Nowicki, A. Abe-Ouchi, A. Aschwanden, H. Choi, J. Fastook, G. Granzow, R. Greve, G. Gutowski, U. Herzfeld, C. Jackson, J. Johnson, C. Khroulev, A. Levermann, W. H. Lipscomb, M. A. Martin, M. Morlighem, B. R. Parizek, D. Pollard, S. F. Price, D. Ren, F. Saito, T. Sato, H. Seddik, H. Seroussi, K. Takahashi, R. Walker, and W. L. Wang, 2013: Ice-sheet model sensitivities to environmental forcing and their use in projecting future sea level (the SeaRISE project). *J. Glaciol.*, **59**, 195-224, doi: 10.3189/2013jog12j125. [[Link](#)]
- Blatter, H., 1995: Velocity and stress fields in grounded glaciers: A simple algorithm for including deviatoric stress gradients. *J. Glaciol.*, **41**, 333-344, doi: 10.3189/s002214300001621x. [[Link](#)]
- Brcic, R., A. Parizzi, M. Eineder, R. Bamler, and F. Meyer, 2011: Ionospheric effects in SAR interferometry: An analysis and comparison of methods for their estimation.

- IGARSS 2011 - 2011 IEEE International Geoscience and Remote Sensing Symposium, Vancouver, BC, Canada, IEEE, doi: 10.1109/igarss.2011.6049351. [\[Link\]](#)
- Cavalié, O., C. Lasserre, M. P. Doin, G. Peltzer, J. Sun, X. Xu, and Z. K. Shen, 2008: Measurement of interseismic strain across the Haiyuan fault (Gansu, China), by InSAR. *Earth Planet. Sci. Lett.*, **275**, 246-257, doi: 10.1016/j.epsl.2008.07.057. [\[Link\]](#)
- Chan, A. K. and C. Peng, 2003: Wavelets for Sensing Technologies, Vol. 1, Artech House, 252 pp.
- Chen, C. W., 2001: Statistical-cost network-flow approaches to two-dimensional phase unwrapping for radar interferometry. Ph.D. Thesis, Stanford University, 141 pp.
- Colgan, W., A. Sommers, H. Rajaram, W. Abdalati, and J. Frahm, 2015: Considering thermal-viscous collapse of the Greenland ice sheet. *Earth's Future*, **3**, 252-267, doi: 10.1002/2015ef000301. [\[Link\]](#)
- Cuffey, K. M. and W. S. B. Paterson, 2010: The Physics of Glaciers, 4th Edition, Academic Press, 704 pp.
- Dee, D. P., S. M. Uppala, A. J. Simmons, P. Berrisford, P. Poli, S. Kobayashi, U. Andrae, M. A. Balmaseda, G. Balsamo, P. Bauer, P. Bechtold, A. C. M. Beljaars, L. van de Berg, J. Bidlot, N. Bormann, C. Delsol, R. Dragani, M. Fuentes, A. J. Geer, L. Haimberger, S. B. Healy, H. Hersbach, E. V. Hólm, L. Isaksen, P. Kållberg, M. Köhler, M. Matricardi, A. P. McNally, B. M. Monge-Sanz, J.-J. Morcrette, B.-K. Park, C. Peubey, P. de Rosnay, C. Tavolato, J.-N. Thépaut, and F. Vitart, 2011: The ERA-Interim reanalysis: Configuration and performance of the data assimilation system. *Q. J. R. Meteorol. Soc.*, **137**, 553-597, doi: 10.1002/qj.828. [\[Link\]](#)
- De Fleurian, B., M. Morlighem, H. Seroussi, E. Rignot, M. R. van den Broeke, P. Kuipers Munneke, J. Mouginot, P. C. J. P. Smeets, and A. J. Tedstone, 2016: A modeling study of the effect of runoff variability on the effective pressure beneath Russell Glacier, West Greenland. *J. Geophys. Res.*, **121**, 1834-1848, doi: 10.1002/2016jf003842. [\[Link\]](#)
- De Zan, F. and A. M. Guarnieri, 2006: TOPSAR: Terrain observation by progressive scans. *IEEE Trans. Geosci. Remote Sensing*, **44**, 2352-2360, doi: 10.1109/tgrs.2006.873853. [\[Link\]](#)
- Ettema, J., M. R. van den Broeke, E. van Meijgaard, W. J. van de Berg, J. L. Bamber, J. E. Box, and R. C. Bales, 2009: Higher surface mass balance of the Greenland ice sheet revealed by high-resolution climate modeling. *Geophys. Res. Lett.*, **36**, doi: 10.1029/2009gl038110. [\[Link\]](#)
- Fitzpatrick, A. A. W., A. Hubbard, I. Joughin, D. J. Quincey, D. Van As, A. P. B. Mikkelsen, S. H. Doyle, B. Hasholt, and G. A. Jones, 2013: Ice flow dynamics and surface meltwater flux at a land-terminating sector of the Greenland ice sheet. *J. Glaciol.*, **59**, 687-696, doi: 10.3189/2013JoG12J143. [\[Link\]](#)
- Gagliardini, O., T. Zwinger, F. Gillet-Chaulet, G. Durand, L. Favier, B. de Fleurian, R. Greve, M. Malinen, C. Martín, P. Råback, J. Ruokolainen, M. Sacchetti, M. Schäfer, H. Seddik, and J. Thies, 2013: Capabilities and performance of Elmer/Ice, a new-generation ice sheet model. *Geosci. Model Dev.*, **6**, 1299-1318, doi: 10.5194/gmd-6-1299-2013. [\[Link\]](#)
- Geudtner, D. and R. Torres, 2012: Sentinel-1 system overview and performance. IGARSS 2012 - 2012 IEEE International Geoscience and Remote Sensing Symposium, Munich, Germany, IEEE, doi: 10.1109/igarss.2012.6351191. [\[Link\]](#)
- Geudtner, D., N. Miranda, I. Navas-Traver, F. C. Vega, P. Prats, N. Yague-Martinez, H. Breit, F. De Zan, Y. Larsen, and A. Recchia, 2018: Sentinel-1A/B SAR and InSAR Performance. EUSAR 2018 - 12th European Conference on Synthetic Aperture Radar, Aachen, Germany, 5 pp.
- Gomba, G., F. R. González, and F. De Zan, 2017: Ionospheric phase screen compensation for the Sentinel-1 TOPS and ALOS-2 ScanSAR modes. *IEEE Trans. Geosci. Remote Sensing*, **55**, 223-235, doi: 10.1109/tgrs.2016.2604461. [\[Link\]](#)
- Gray, A. L., K. E. Mattar, P. W. Vachon, R. Bindenschadler, K. C. Jezek, R. Forster, and J. P. Crawford, 1998: InSAR results from the RADARSAT Antarctic Mapping Mission data: Estimation of glacier motion using a simple registration procedure. IGARSS '98, Sensing and Managing the Environment, 1998 IEEE International Geoscience and Remote Sensing, Symposium Proceedings, Cat. No.98CH36174, IEEE, Seattle, WA, USA, 1638-1640, doi: 10.1109/IGARSS.1998.691662. [\[Link\]](#)
- Gray, A. L., N. Short, K. E. Mattar, and K. C. Jezek, 2001: Velocities and flux of the Filchner Ice Shelf and its tributaries determined from speckle tracking interferometry. *Can. J. Rem. Sens.*, **27**, 193-206, doi: 10.1080/07038992.2001.10854936. [\[Link\]](#)
- Hanna, E., P. Huybrechts, K. Steffen, J. Cappelen, R. Huff, C. Shuman, T. Irvine-Fynn, S. Wise, and M. Griffiths, 2008: Increased runoff from melt from the Greenland Ice Sheet: A response to global warming. *J. Climate*, **21**, 331-341, doi: 10.1175/2007jcli1964.1. [\[Link\]](#)
- Hanna, E., F. J. Navarro, F. Pattyn, C. M. Domingues, X. Fettweis, E. R. Ivins, R. J. Nicholls, C. Ritz, B. Smith, S. Tulaczyk, P. L. Whitehouse, and H. J. Zwally, 2013: Ice-sheet mass balance and climate change. *Nature*, **498**, 51-59, doi: 10.1038/nature12238. [\[Link\]](#)
- Hanssen, R. F., 2001: Radar Interferometry: Data Interpretation and Error Analysis, Springer Netherlands, 308 pp, doi: 10.1007/0-306-47633-9. [\[Link\]](#)
- Heid, T. and A. Käab, 2012: Evaluation of existing image matching methods for deriving glacier surface displacements globally from optical satellite imagery.

- Remote Sens. Environ.*, **118**, 339-355, doi: 10.1016/j.rse.2011.11.024. [[Link](#)]
- Henderson, F. M. and A. J. Lewis, 1998: Principles and Applications of Imaging Radar, Manual of Remote Sensing, Volume 2, John Wiley and Sons, 896 pp.
- Huang, L. and Z. Li, 2011: Comparison of SAR and optical data in deriving glacier velocity with feature tracking. *Int. J. Remote Sens.*, **32**, 2681-2698, doi: 10.1080/01431161003720395. [[Link](#)]
- Jevrejeva, S., A. Grinsted, and J. C. Moore, 2014: Upper limit for sea level projections by 2100. *Environ. Res. Lett.*, **9**, 104008, doi: 10.1088/1748-9326/9/10/104008. [[Link](#)]
- Jolivet, R., R. Grandin, C. Lasserre, M. P. Doin, and G. Peltzer, 2011: Systematic InSAR tropospheric phase delay corrections from global meteorological reanalysis data. *Geophys. Res. Lett.*, **38**, doi: 10.1029/2011gl048757. [[Link](#)]
- Joughin, I., S. B. Das, M. A. King, B. E. Smith, I. M. Howat, and T. Moon, 2008: Seasonal speedup along the western flank of the Greenland Ice Sheet. *Science*, **320**, 781-783, doi: 10.1126/science.1153288. [[Link](#)]
- Joughin, I., B. E. Smith, I. M. Howat, T. Scambos, and T. Moon, 2010: Greenland flow variability from ice-sheet-wide velocity mapping. *J. Glaciol.*, **56**, 415-430, doi: 10.3189/002214310792447734. [[Link](#)]
- Joughin, I., B. E. Smith, I. M. Howat, T. Moon, and T. A. Scambos, 2016: A SAR record of early 21st century change in Greenland. *J. Glaciol.*, **62**, 62-71, doi: 10.1017/jog.2016.10. [[Link](#)]
- Kääb, A., C. Huggel, F. Paul, R. Wessels, B. Raup, H. Kieffer, and J. Kargel, 2002: Glacier Monitoring from ASTER Imagery: Accuracy and Applications. Proceedings of EARSeL-LISSIG-Workshop Observing our Cryosphere from Space.
- Karpilo, R. D., 2009: Glacier monitoring techniques. In: Young, R. and L. Norby (Eds.), Geological Monitoring, The Geological Society of America, Boulder, Colorado, 141-162, doi: 10.1130/2009.monitoring(06). [[Link](#)]
- Ke, C.-Q., C. Kou, R. Ludwig, and X. Qin, 2013: Glacier velocity measurements in the eastern Yigong Zangbo basin, Tibet, China. *J. Glaciol.*, **59**, 1060-1068, doi: 10.3189/2013jog12j234. [[Link](#)]
- Khan, S. A., K. H. Kjær, M. Bevis, J. L. Bamber, J. Wahr, K. K. Kjeldsen, A. A. Bjørk, N. J. Korsgaard, L. A. Stearns, M. R. van den Broeke, L. Liu, N. K. Larsen, and I. S. Muresan, 2014: Sustained mass loss of the northeast Greenland ice sheet triggered by regional warming. *Nat. Clim. Change*, **4**, 292-299, doi: 10.1038/nclimate2161. [[Link](#)]
- Korona, J., E. Berthier, M. Bernard, F. Rémy, and E. Thouvenot, 2009: SPIRIT. SPOT 5 stereoscopic survey of polar ice: Reference images and topographies during the fourth International Polar Year (2007–2009). *ISPRS J. Photogram. Rem. Sens.*, **64**, 204-212, doi: 10.1016/j.isprsjprs.2008.10.005. [[Link](#)]
- Kraaijenbrink, P., S. W. Meijer, J. M. Shea, F. Pellicciotti, S. M. De Jong, and W. W. Immerzeel, 2016: Seasonal surface velocities of a Himalayan glacier derived by automated correlation of unmanned aerial vehicle imagery. *Ann. Glaciol.*, **57**, 103-113, doi: 10.3189/2016aog71a072. [[Link](#)]
- Larour, E., H. Seroussi, M. Morlighem, and E. Rignot, 2012: Continental scale, high order, high spatial resolution, ice sheet modeling using the Ice Sheet System Model (ISSM). *J. Geophys. Res.*, **117**, doi: 10.1029/2011jf002140. [[Link](#)]
- Larour, E., J. Utke, B. Csatho, A. Schenk, H. Seroussi, M. Morlighem, E. Rignot, N. Schlegel, and A. Khazendar, 2014: Inferred basal friction and surface mass balance of the Northeast Greenland Ice Stream using data assimilation of ICESat (Ice Cloud and land Elevation Satellite) surface altimetry and ISSM (Ice Sheet System Model). *The Cryosphere*, **8**, 2335-2351, doi: 10.5194/tc-8-2335-2014. [[Link](#)]
- Leprince, S., S. Barbot, F. Ayoub, and J.-P. Avouac, 2007: Automatic and precise orthorectification, coregistration, and subpixel correlation of satellite images, application to ground deformation measurements. *IEEE Trans. Geosci. Remote Sensing*, **45**, 1529-1558, doi: 10.1109/tgrs.2006.888937. [[Link](#)]
- Lindbäck, K. and R. Pettersson, 2015: Spectral roughness and glacial erosion of a land-terminating section of the Greenland Ice Sheet. *Geomorphology*, **238**, 149-159, doi: 10.1016/j.geomorph.2015.02.027. [[Link](#)]
- López-Quiroz, P., M.-P. Doin, F. Tupin, P. Briole, and J.-M. Nicolas, 2009: Time series analysis of Mexico City subsidence constrained by radar interferometry. *J. Appl. Geophys.*, **69**, 1-15, doi: 10.1016/j.jappgeo.2009.02.006. [[Link](#)]
- MacAyeal, D. R., 1989: Large-scale ice flow over a viscous basal sediment: Theory and application to ice stream B, Antarctica. *J. Geophys. Res.*, **94**, 4071-4087, doi: 10.1029/jb094ib04p04071. [[Link](#)]
- MacAyeal, D. R., 1992: The basal stress distribution of Ice Stream E, Antarctica, inferred by control methods. *J. Geophys. Res.*, **97**, 595-603, doi: 10.1029/91jb02454. [[Link](#)]
- Malenovský, Z., H. Rott, J. Cihlar, M. E. Schaepman, G. García-Santos, R. Fernandes, and M. Berger, 2012: Sentinels for science: Potential of Sentinel-1, -2, and -3 missions for scientific observations of ocean, cryosphere, and land. *Remote Sens. Environ.*, **120**, 91-101, doi: 10.1016/j.rse.2011.09.026. [[Link](#)]
- Massonnet, D. and K. L. Feigl, 1998: Radar interferometry and its application to changes in the Earth's surface. *Rev. Geophys.*, **36**, 441-500, doi: 10.1029/97rg03139. [[Link](#)]

- Mattar, K. E., P. W. Vachon, D. Geudtner, A. L. Gray, I. G. Cumming, and M. Brugman, 1998: Validation of alpine glacier velocity measurements using ERS tandem-mission SAR data. *IEEE Trans. Geosci. Remote Sensing*, **36**, 974-984, doi: 10.1109/36.673688. [[Link](#)]
- Mätzler, C., 1987: Applications of the interaction of microwaves with the natural snow cover. *Rem. Sens. Rev.*, **2**, 259-387, doi: 10.1080/02757258709532086. [[Link](#)]
- Meta, A., J. Mittermayer, P. Prats, R. Scheiber, and U. Steinbrecher, 2010: TOPS imaging with TerraSAR-X: Mode design and performance analysis. *IEEE Trans. Geosci. Remote Sensing*, **48**, 759-769, doi: 10.1109/tgrs.2009.2026743. [[Link](#)]
- Michel, R. and E. Rignot, 1999: Flow of Glaciario Moreno, Argentina, from repeat-pass Shuttle Imaging Radar images: Comparison of the phase correlation method with radar interferometry. *J. Glaciol.*, **45**, 93-100, doi: 10.3189/s002214300003075. [[Link](#)]
- Moon, T., I. Joughin, B. Smith, and I. Howat, 2012: 21st-century evolution of Greenland outlet glacier velocities. *Science*, **336**, 576-578, doi: 10.1126/science.1219985. [[Link](#)]
- Morlighem, M., E. Rignot, H. Seroussi, E. Larour, H. Ben Dhia, and D. Aubry, 2010: Spatial patterns of basal drag inferred using control methods from a full-Stokes and simpler models for Pine Island Glacier, West Antarctica. *Geophys. Res. Lett.*, **37**, doi: 10.1029/2010gl043853. [[Link](#)]
- Morlighem, M., E. Rignot, J. Mouginot, X. Wu, H. Seroussi, E. Larour, and J. Paden, 2013: High-resolution bed topography mapping of Russell Glacier, Greenland, inferred from Operation IceBridge data. *J. Glaciol.*, **59**, 1015-1023, doi: 10.3189/2013JoG12J235. [[Link](#)]
- Morlighem, M., E. Rignot, J. Mouginot, H. Seroussi, and E. Larour, 2014: Deeply incised submarine glacial valleys beneath the Greenland ice sheet. *Nat. Geosci.*, **7**, 418-422, doi: 10.1038/ngeo2167. [[Link](#)]
- Morlighem, M., E. Rignot, J. Mouginot, H. Seroussi, and E. Larour, 2015: IceBridge BedMachine Greenland, Version 2, NASA NSIDC DAAC: NASA National Snow and Ice Data Center Distributed Active Archive Center, Boulder, Colorado USA, doi: 10.5067/AD7B-0HQNSJ29. [[Link](#)]
- Nagler, T., H. Rott, M. Hetzenecker, J. Wuite, and P. Potin, 2015: The Sentinel-1 mission: New opportunities for ice sheet observations. *Remote Sens.*, **7**, 9371-9389, doi: 10.3390/rs70709371. [[Link](#)]
- Nagler, T., H. Rott, E. Ripper, G. Bippus, and M. Hetzenecker, 2016: Advancements for Snowmelt Monitoring by Means of Sentinel-1 SAR. *Remote Sens.*, **8**, 348, doi: 10.3390/rs8040348. [[Link](#)]
- Nicholls, R. J., S. E. Hanson, J. A. Lowe, R. A. Warrick, X. Lu, and A. J. Long, 2014: Sea-level scenarios for evaluating coastal impacts. *WIREs Clim. Change*, **5**, 129-150, doi: 10.1002/wcc.253. [[Link](#)]
- Palmer, S., A. Shepherd, P. Nienow, and I. Joughin, 2011: Seasonal speedup of the Greenland Ice Sheet linked to routing of surface water. *Earth Planet. Sci. Lett.*, **302**, 423-428, doi: 10.1016/j.epsl.2010.12.037. [[Link](#)]
- Pattyn, F., 1999: DInSAR and coherence tracking applied to glaciology: The example of Shirase Glacier. FRINGE'99 Workshop, Advancing ERS-SAR Interferometry from Applications Towards Operations, Liège, Belgium.
- Pattyn, F., 2003: A new three-dimensional higher-order thermomechanical ice sheet model: Basic sensitivity, ice stream development, and ice flow across subglacial lakes. *J. Geophys. Res.*, **108**, doi: 10.1029/2002jb002329. [[Link](#)]
- Peppas, M. V., J. P. Mills, P. Moore, P. E. Miller, and J. E. Chambers, 2017: Brief communication: Landslide motion from cross correlation of UAV-derived morphological attributes. *Nat. Hazards Earth Syst. Sci.*, **17**, 2143-2150, doi: 10.5194/nhess-17-2143-2017. [[Link](#)]
- Pritchard, H. D., R. J. Arthern, D. G. Vaughan, and L. A. Edwards, 2009: Extensive dynamic thinning on the margins of the Greenland and Antarctic ice sheets. *Nature*, **461**, 971-975, doi: 10.1038/nature08471. [[Link](#)]
- Quincey, D. J., R. M. Lucas, S. D. Richardson, N. F. Glasser, M. J. Hambrey, and J. M. Reynolds, 2005: Optical remote sensing techniques in high-mountain environments: Application to glacial hazards. *Prog. Phys. Geogr.*, **29**, 475-505, doi: 10.1191/0309133305pp456ra. [[Link](#)]
- Rathje, E. M., S. S. Secara, J. G. Martin, S. van Ballegooy, and J. Russell, 2017: Liquefaction-Induced Horizontal Displacements from the Canterbury Earthquake Sequence in New Zealand Measured from Remote Sensing Techniques. *Earthq. Spectra*, **33**, 1475-1494, doi: 10.1193/080816eqs127m. [[Link](#)]
- Rennermalm, A. K., L. C. Smith, V. W. Chu, J. E. Box, R. R. Forster, M. R. Van den Broeke, D. Van As, and S. E. Moustafa, 2013: Evidence of meltwater retention within the Greenland ice sheet. *The Cryosphere*, **7**, 1433-1445, doi: 10.5194/tc-7-1433-2013. [[Link](#)]
- Rignot, E. and J. Mouginot, 2012: Ice flow in Greenland for the International Polar Year 2008-2009. *Geophys. Res. Lett.*, **39**, doi: 10.1029/2012gl051634. [[Link](#)]
- Robin, G., 1976: Is the basal ice of a temperate glacier at the pressure melting point? *J. Glaciol.*, **16**, 183-196, doi: 10.1017/s002214300003152x. [[Link](#)]
- Robson, B. A., C. Nuth, S. O. Dahl, D. Hölbling, T. Strozzi, and P. R. Nielsen, 2015: Automated classification of debris-covered glaciers combining optical, SAR and topographic data in an object-based environment. *Remote Sens. Environ.*, **170**, 372-387, doi: 10.1016/j.rse.2015.10.001. [[Link](#)]
- Rosen, P. A., S. Hensley, G. Peltzer, and M. Simons, 2004: Updated repeat orbit interferometry package released.

- Eos, Trans. AGU*, **85**, 47, doi: 10.1029/2004eo050004. [[Link](#)]
- Sánchez-Gómez, P. and F. Navarro, 2017: Glacier surface velocity retrieval using D-InSAR and offset tracking techniques applied to ascending and descending passes of Sentinel-1 data for southern Ellesmere ice caps, Canadian Arctic. *Remote Sens.*, **9**, 442, doi: 10.3390/rs9050442. [[Link](#)]
- Shepherd, A., E. R. Ivins, G. A. V. R. Barletta, M. J. Bentley, S. Bettadpur, K. H. Briggs, D. H. Bromwich, R. Forsberg, N. Galin, M. Horwath, S. Jacobs, I. Joughin, M. A. King, J. T. M. Lenaerts, J. Li, S. R. M. Ligtenberg, A. Luckman, S. B. Luthcke, M. McMillan, R. Meister, G. Milne, J. Mouginot, A. Muir, J. P. Nicolas, J. Paden, A. J. Payne, H. Pritchard, E. Rignot, H. Rott, L. S. Sorensen, T. A. Scambos, B. Scheuchl, E. J. O. Schrama, B. Smith, A. V. Sundal, J. H. van Angelen, W. J. van de Berg, M. R. van den Broeke, D. G. Vaughan, I. Velicogna, J. Wahr, P. L. Whitehouse, D. J. Wingham, D. Yi, D. Young, and H. J. Zwally, 2012: A reconciled estimate of ice-sheet mass balance. *Science*, **338**, 1183-1189, doi: 10.1126/science.1228102. [[Link](#)]
- Shi, J. and J. Dozier, 1995: Inferring snow wetness using C-band data from SIR-C's polarimetric synthetic aperture radar. *IEEE Trans. Geosci. Remote Sensing*, **33**, 905-914, doi: 10.1109/36.406676. [[Link](#)]
- Smith, L. C., V. W. Chu, K. Yang, C. J. Gleason, L. H. Pitcher, A. K. Rennermalm, C. J. Legleiter, A. E. Behar, B. T. Overstreet, S. E. Moustafa, M. Tedesco, R. R. Forster, A. L. LeWinter, D. C. Finnegan, Y. Sheng, and J. Balog, 2015: Efficient meltwater drainage through supraglacial streams and rivers on the southwest Greenland ice sheet. *Proc. Natl. Acad. Sci.*, **112**, 1001-1006, doi: 10.1073/pnas.1413024112. [[Link](#)]
- Sole, A., P. Nienow, I. Bartholomew, D. Mair, T. Cowton, A. Tedstone, and M. A. King, 2013: Winter motion mediates dynamic response of the Greenland Ice Sheet to warmer summers. *Geophys. Res. Lett.*, **40**, 3940-3944, doi: 10.1002/grl.50764. [[Link](#)]
- Storey, J., M. Choate, and K. Lee, 2014: Landsat 8 Operational Land Imager on-orbit geometric calibration and performance. *Remote Sens.*, **6**, 11127-11152, doi: 10.3390/rs61111127. [[Link](#)]
- Strozzi, T., U. Wegmuller, and C. Matzler, 1999: Mapping wet snowcovers with SAR interferometry. *Int. J. Remote Sens.*, **20**, 2395-2403, doi: 10.1080/014311699212083. [[Link](#)]
- Strozzi, T., A. Luckman, T. Murray, U. Wegmuller, and C. L. Werner, 2002: Glacier motion estimation using SAR offset-tracking procedures. *IEEE Trans. Geosci. Remote Sensing*, **40**, 2384-2391, doi: 10.1109/tgrs.2002.805079. [[Link](#)]
- Strozzi, T., A. Kouraev, A. Wiesmann, U. Wegmüller, A. Sharov, and C. Werner, 2008: Estimation of Arctic glacier motion with satellite L-band SAR data. *Remote Sens. Environ.*, **112**, 636-645, doi: 10.1016/j.rse.2007.06.007. [[Link](#)]
- Tedstone, A. J., P. W. Nienow, N. Gourmelen, and A. J. Sole, 2014: Greenland ice sheet annual motion insensitive to spatial variations in subglacial hydraulic structure. *Geophys. Res. Lett.*, **41**, 8910-8917, doi: 10.1002/2014gl062386. [[Link](#)]
- Thomsen, H. H., L. Thorning, and R. J. Braithwaite, 1988: Glacier-Hydrological conditions on the inland ice North-East of Jakobshavn, Ilusissat, West Greenland, Grønlands Geologiske Undersøgelse, Report, 138.
- Torres, R., P. Snoeij, D. Geudtner, D. Bibby, M. Davidson, E. Attema, P. Potin, B. Rommen, N. Floury, M. Brown, I. N. Traver, P. Deghaye, B. Duesmann, B. Rosich, N. Miranda, C. Bruno, M. L'Abbate, R. Croci, A. Pietropaolo, M. Huchler, and F. Rostan, 2012: GMES Sentinel-1 mission. *Remote Sens. Environ.*, **120**, 9-24, doi: 10.1016/j.rse.2011.05.028. [[Link](#)]
- Tsai, Y.-L., S.-Y. Lin, and J.-R. Kim, 2018: Tracking Greenland Russell Glacier Movements Using Pixel-offset Method. *J. Photogram. Rem. Sens.*, **23**, 173-189, doi: 10.6574/JPRS.201809\_23(3).0003. [[Link](#)]
- Tsai, Y.-L. S., A. Dietz, N. Oppelt, and C. Kuenzer, 2019: Wet and Dry Snow Detection Using Sentinel-1 SAR Data for Mountainous Areas with a Machine Learning Technique. *Remote Sens.*, **11**, 895, doi: 10.3390/rs11080895. [[Link](#)]
- Ulaby, F. T., R. K. Moore, and A. K. Fung, 1986: Microwave Remote Sensing: Active and Passive, Vol. 3, From Theory to Applications, Artech House, 1116 pp.
- Van de Wal, R. S. W., W. Boot, M. R. van den Broeke, C. J. P. P. Smeets, C. H. Reijmer, J. J. A. Donker, and J. Oerlemans, 2008: Large and rapid melt-induced velocity changes in the ablation zone of the Greenland ice sheet. *Science*, **321**, 111-113, doi: 10.1126/science.1158540. [[Link](#)]
- Weidick, A., 1995: Satellite image atlas of glaciers of the world: Greenland. U.S. Geological Survey Professional Paper 1386-C, United States Government Printing Office, Washington.
- Zebker, H. A. and J. Villasenor, 1992: Decorrelation in interferometric radar echoes. *IEEE Trans. Geosci. Remote Sensing*, **30**, 950-959, doi: 10.1109/36.175330. [[Link](#)]
- Zhou, J., Z. Li, X. Li, S. Liu, Q. Chen, C. Xie, and B. Tian, 2011: Movement estimate of the Dongkemadi Glacier on the Qinghai-Tibetan Plateau using L-band and C-band spaceborne SAR data. *Int. J. Remote Sens.*, **32**, 6911-6928, doi: 10.1080/01431161.2010.517225. [[Link](#)]
- Zwally, H. J., W. Abdalati, T. Herring, K. Larson, J. Saba, and K. Steffen, 2002: Surface melt-induced acceleration of Greenland ice-sheet flow. *Science*, **297**, 218-222, doi: 10.1126/science.1072708. [[Link](#)]

## APPENDIX A.

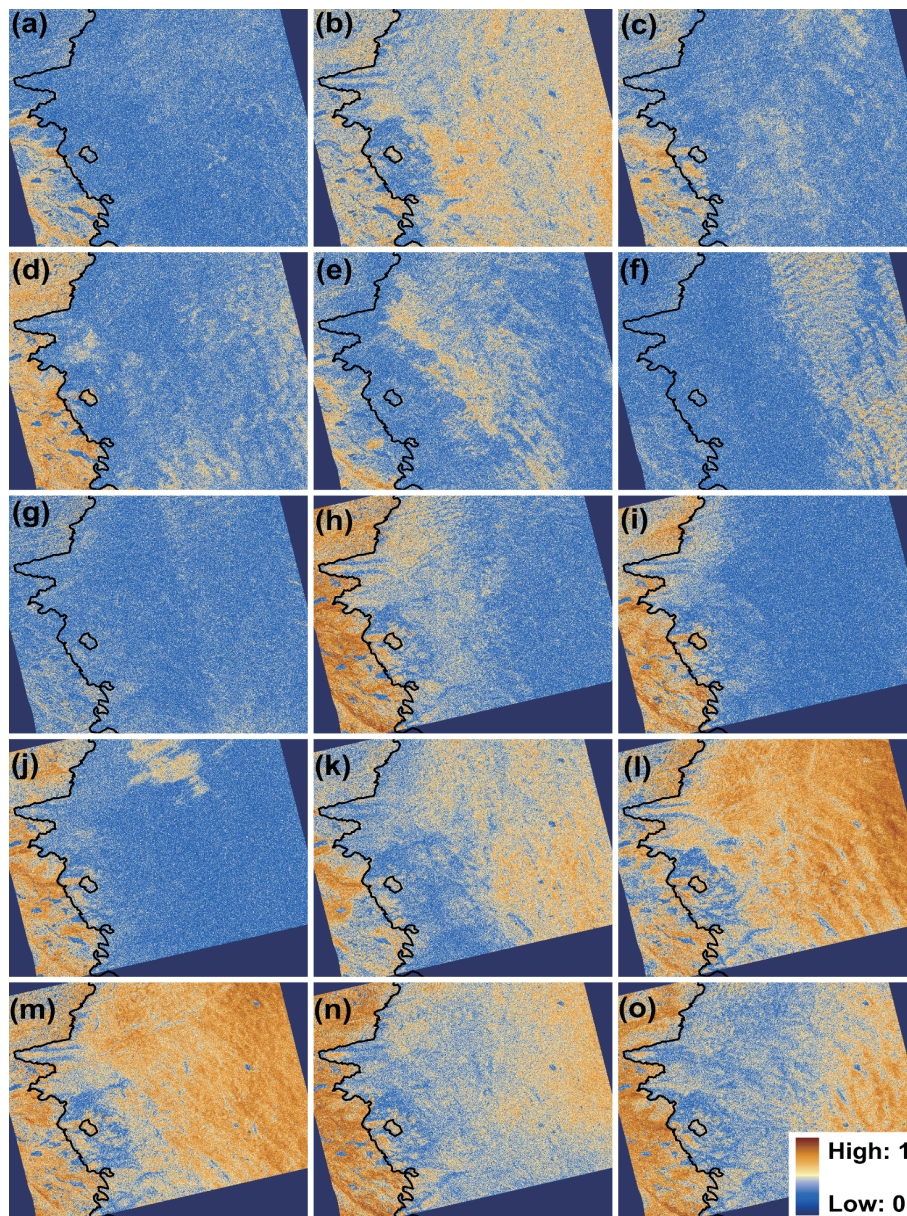


Fig. A1. The temporal coherence map of each wintertime InSAR time-series pair. (a) 2016/9/30 - 2016/10/6; (b) 2016/10/6 - 2016/10/12; (c) 2016/10/12 - 2016/10/18; (d) 2016/10/18 - 2016/10/24; (e) 2016/10/24 - 2016/10/30; (f) 2016/10/30 - 2016/11/5; (g) 2016/11/5 - 2016/11/11; (h) 2016/11/11 - 2016/11/17; (i) 2016/11/17 - 2016/11/23; (j) 2016/11/23 - 2016/11/29; (k) 2016/11/29 - 2016/12/5; (l) 2016/12/5 - 2016/12/11; (m) 2016/12/11 - 2016/12/17; (n) 2016/12/17 - 2016/12/23; (o) 2016/12/23 - 2016/12/29.